Title
Towards robust laser beam propagation in atmospheric turbulence

Journal
Photonics Research, 14(7)

ISSN
2327-9125

Authors
Zhang, Boyu
Kim, Changmin
Li, Wenzhe
et al.

Publication Date
2026-07-01

DOI
10.1364/prj.591185

Research Article Vol. 14, No. 7 / July 2026 / Photonics Research 3245

PHOTONICS Research

Towards robust laser beam propagation in atmospheric turbulence

Boyu Zhang,[1,2,†] Changmin Kim,[1,2,†] Wenzhe Li,[2] Jose Chirinos,[2] Xianglei Mao,[2] Richard Harrison,[2] and Vassilia Zorba[1,2,*]

[1]Department of Mechanical Engineering, University of California at Berkeley, Berkeley, California 94720, USA
[2]Laser Technologies Group, Energy Technologies Area, Lawrence Berkeley National Laboratory, Berkeley, California 94720, USA
[†]These authors contributed equally to this work.
*Corresponding author: vzorba@lbl.gov

Received 21 January 2026; revised 30 April 2026; accepted 19 May 2026; posted 20 May 2026 (Doc. ID 591185); published 1 July 2026

High-fidelity optical propagation through the atmosphere is essential for free-space optical technologies, including laser-based remote sensing and optical communication. However, atmospheric turbulence severely distorts beams and compromises system performance. In this work, we employ hypergeometric-Gaussian (HyGG) vortex beams as probes to characterize and mitigate atmospheric turbulence. Using over 250,000 experimental and simulated frames, we show that refining the power spectrum density (PSD) can reduce numerical prediction errors by up to 79.8%. Concurrently, experimental observations supported by numerical simulations demonstrate that HyGG beams exhibit superior turbulence resilience across multiple metrics compared to conventional Gaussian beams, particularly in their ability to withstand over 5 times stronger turbulence while maintaining similar intensity fluctuations. These dual investigations, on both turbulence mitigation and robust beam solutions, converge to form a unified strategy for enhancing free-space optical system performance. Collectively, our findings provide new insights into light–turbulence interactions and highlight the practical utility of vortex beams under atmospheric conditions.

https://doi.org/10.1364/PRJ.591185

1. INTRODUCTION

Active laser-based remote sensing techniques, including light detection and ranging (LiDAR) [1,2], laser-induced breakdown spectroscopy (LIBS) [3], laser-induced fluorescence (LIF) [4], and Raman spectroscopy [5], have been widely used for remote characterization of gas, liquid, aerosols, and solid materials. In such applications, highly directional, low-divergence laser beams enable concentrated power projection and stable detection from standoff distances. These capabilities are crucial in scenarios requiring long-range monitoring and the management of resources, pollutants, or hazardous materials, particularly in environmental disaster responses and operations under extreme conditions. Conventional Gaussian beams have been extensively used in applications such as topographic mapping [1,2], environmental monitoring [6,7], geological and planetary exploration [8–10], and detection of radiological substances [11]. However, their performance degrades substantially under atmospheric turbulence, resulting in beam quality deterioration and intensity fluctuations [12,13].

To overcome these limitations, vortex beams carrying orbital angular momentum (OAM) have been proposed as a promising approach for turbulence effect mitigation [14–16]. Prior numerical and theoretical studies have reported that vortex beams exhibit improved propagation characteristics over Gaussian beams, as evidenced by reduced scintillation indices [17,18] and greater resilience to intensity profile distortion [19]. Yet, most of these investigations rely solely on simulations, with limited experimental validation constrained by short propagation distances, simplified turbulence models, or a lack of quantitative metrics.

To bridge the gap between theoretical promise and real-world application, we present a comprehensive experimental and numerical study that evaluates OAM beam propagation over 100 m through localized strong turbulence with topological charges 0 (conventional Gaussian beam), 1, and 2. The turbulence is generated by a high-power air-mixing system with a power output of 4000 W/m, producing refractive index structure parameter C_n^2 up to the order of 10^{-9} $\mathrm{m}^{-2/3}$, which indicates severe turbulence conditions such as those found in jet engine exhaust flows [20–22].

To quantitatively evaluate how different beams respond to such turbulence, we employ four quantitative metrics: ellipticity and eccentricity to evaluate the preservation of beam circularity, and the scintillation index and vortex degradation to quantify energy stability and structural integrity. Numerical simulations and experimental measurements consistently

2327-9125/26/073245-23 Journal © 2026 Chinese Laser Press

demonstrate that higher-order vortex beams exhibit superior performance in maintaining beam shape and propagation stability under turbulent conditions.

Beyond evaluating beam performance, this study presents the first integrated experimental and numerical investigation of vortex beam circularity as a novel and practical diagnostic for evaluating turbulence models. This approach is motivated by the growing interest in OAM states for strengthening various free-space optical applications, such as free-space optical (FSO) communications [23–25], where the interaction between OAM beams and turbulence plays a crucial role in determining practical system performance [26–29]. Therefore, a comprehensive understanding and accurate modeling of turbulence effects is critical. Turbulence modeling typically relies on power spectral density (PSD) functions of refractive index fluctuations, such as Kolmogorov, Tatarskii, or modified von Kármán (mvK) spectra, as summarized in Table 1 [30–41].

While widely adopted, the accuracy, applicability, and limitations of these PSD models have not been systematically validated against experimental observations. In addition, the selection of a particular PSD model is often presented without explicit justification or comparison with alternative models. In this work, we utilize beam circularity as an experimental probe to evaluate the predictive performance of different PSD models. Our findings show that turbulence strength estimates derived from different PSD formulations can differ by up to a factor of 2. Moreover, selecting an appropriate PSD model can reduce numerical prediction error in beam circularity under turbulence by as much as 79.8%, which is crucial for accurate modeling of light propagation, of which the significance can be extended to various fields involving complex media modeled by Kolmogorov's theory of turbulence, including adaptive optics, atmosphere-penetrating imaging, and directed energy systems.

2. RESULTS

A. Experiments of 100 m Beam Propagation in Turbulence

The experimental setup to measure the dynamic change of the beam characteristics in turbulence is shown in Fig. 1(a). Vortex beams are generated by switching in vortex retarders of the corresponding order mounted in flipping holders. This configuration mimics a scenario in which a highly turbulent region obstructs direct access to a distant target, making robust energy delivery over long distances essential.

Snapshots of the conventional Gaussian beam ($m = 0$) and vortex beams with topological charges $m = 1, 2$ were captured by the beam profiler, as shown in Fig. 1(b). The horizontal scale of each image is 106.5 mm. As the turbulence strength increases, the profiles of all beams vary more pronouncedly in time, showcasing the distortion effects imposed by turbulence. The dynamic change of beam shapes can be seen in Visualization 1, Visualization 2, Visualization 3, Visualization 4, Visualization 5, Visualization 6, Visualization 7, Visualization 8, Visualization 9, Visualization 10, Visualization 11, Visualization 12, Visualization 13, Visualization 14, and Visualization 15, which correspond to the three topological charges ($m = 0, 1, 2$) and five turbulence strengths from $C_n^2 = 7.19 \times 10^{-15}\ \mathrm{m}^{-2/3}$ to $1.07 \times 10^{-9}\ \mathrm{m}^{-2/3}$. While these visual distortions qualitatively reflect the impact of turbulence, rigorous assessment demands precise quantification of turbulence strength in these C_n^2 values. The following section outlines how turbulence was quantified in these experiments, forming the basis for evaluating beam performance in atmospheric propagation.

It is worth emphasizing that the generated vortex beams correspond to the hypergeometric–Gaussian (HyGG) mode, of which the electric field at the source plane is given by

$$E_m(r, \varphi, z = 0) = E_0 \left(\frac{r}{w_0}\right)^{p+|m|} \exp\left[-\left(\frac{r}{w_0}\right)^2 + im\varphi\right] = E_0 \exp\left[-\left(\frac{r}{w_0}\right)^2 + im\varphi\right], \tag{1}$$

where (r, φ, z) are the cylindrical coordinates, i is the complex number imaginary unit, w_0 is the waist radius, m is the topological charge, and $p = -|m|$ since there is only phase modulation at the source plane [42]. Here, m is taken as a non-negative integer, and the beam reduces to a conventional Gaussian beam when $m = 0$. For propagation in a non-disturbed environment, an analytical expression of the complex field of this HyGG mode is given by

Table 1. Examples of PSD Models Adopted in Turbulence Modeling

Ref.	PSD	Application
[30]	Kolmogorov	Assessment of phase distortion compensation in atmospheric propagation using deep learning
[31]	Kolmogorov	Deriving the specific expression for different FSO time and frequency transfer techniques
[32]	Kolmogorov	Introducing more generalized perturbations for investigating the vectorness of structured light
[33]	Tatarskii	Evaluating the fiber-coupling efficiency of partially coherent flat-topped beam propagation through a turbulent atmosphere
[34]	Tatarskii	Studying the angular width and the M^2-factor of partially coherent Airy beams in atmospheric turbulence
[35]	mvK	Modeling the performance of bidirectional ground-space optical link corrected by adaptive optics
[36]	mvK	Numerical evaluation of intensity fluctuation to estimate the maximum propagation distance under a given level of beam scintillation in an urban environment
[37]	mvK	Simulation of a temporally dynamic atmospheric wavefront in atmospheric turbulence
[38]	mvK	Numerical demonstration of the atmospheric turbulence effects on different kinds of vortex beams
[39]	mvK	Emulation of turbulence effects and validation of the proposed robustness enhancement framework via active convolved illumination
[40]	mvK	Testing the effectiveness of astigmatic transformations for OAM mode identification in atmospheric turbulence
[41]	mvK	Emulation of a turbulent environment where optical chaotic signal is recovered by a programmable optical processor

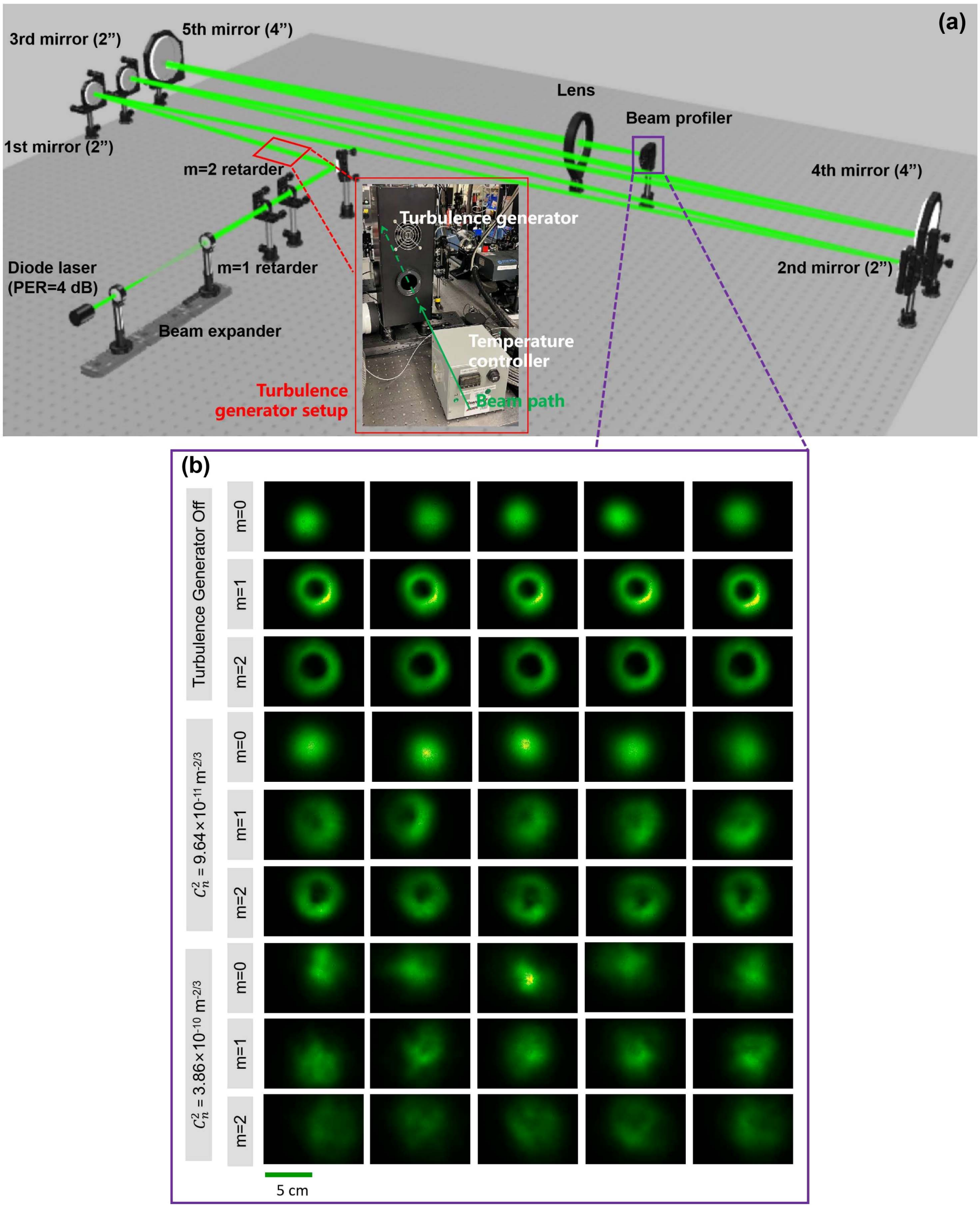

Fig. 1. Experimental setup and captured beam profiles. (a) Schematic diagram of the 100 m propagation setup. The position of the turbulence generator in the beam path is indicated by the red rectangle. The inset shows the turbulence generator with the temperature control unit. (b) Experimentally measured snapshots of beams with different topological charges under varying turbulent strengths after 100 m propagation. The five images in the same row are five randomly selected replicas to reflect the distortion effects of turbulence.

$$E_m(r,\varphi,z) = \sqrt{\frac{2^{\frac{m}{2}+1}}{\pi\Gamma(\frac{m}{2}+1)}}\frac{\Gamma\left(\frac{m}{2}+1\right)}{\Gamma(m+1)} i^{m+1}\left(\frac{z}{z_R}\right)^{-\frac{m}{2}} \times \left(\frac{z}{z_R}+i\right)^{-(\frac{m}{2}+1)}\left(\frac{r}{w_0}\right)^{m}\exp\left[-\frac{i}{\frac{z}{z_R}+i}\left(\frac{r}{w_0}\right)^2\right] \times \exp(im\varphi)\,{}_1F_1\left[\frac{m}{2}, m+1, \frac{\left(\frac{r}{w_0}\right)^2}{\frac{z}{z_R}\left(\frac{z}{z_R}+i\right)}\right], \tag{2}$$

where $z_R = \pi w_0^2/\lambda$ is the Rayleigh range, λ is the wavelength, Γ is the gamma function, and ${}_1F_1$ is the confluent hypergeometric function [42–44]. As shown in Fig. 2, the beam categorization was confirmed by the beam profile evolution against the propagation distance since the sizes of the annular (doughnut) beam inner diameter for the HyGG modes were zero at the source plane and grew larger during propagation. This feature distinguishes the HyGG mode from other widely studied vortex beam modes, such as the Laguerre–Gaussian (LG) mode. Therefore, unless otherwise specified, vortex beams refer to HyGG modes throughout the following content.

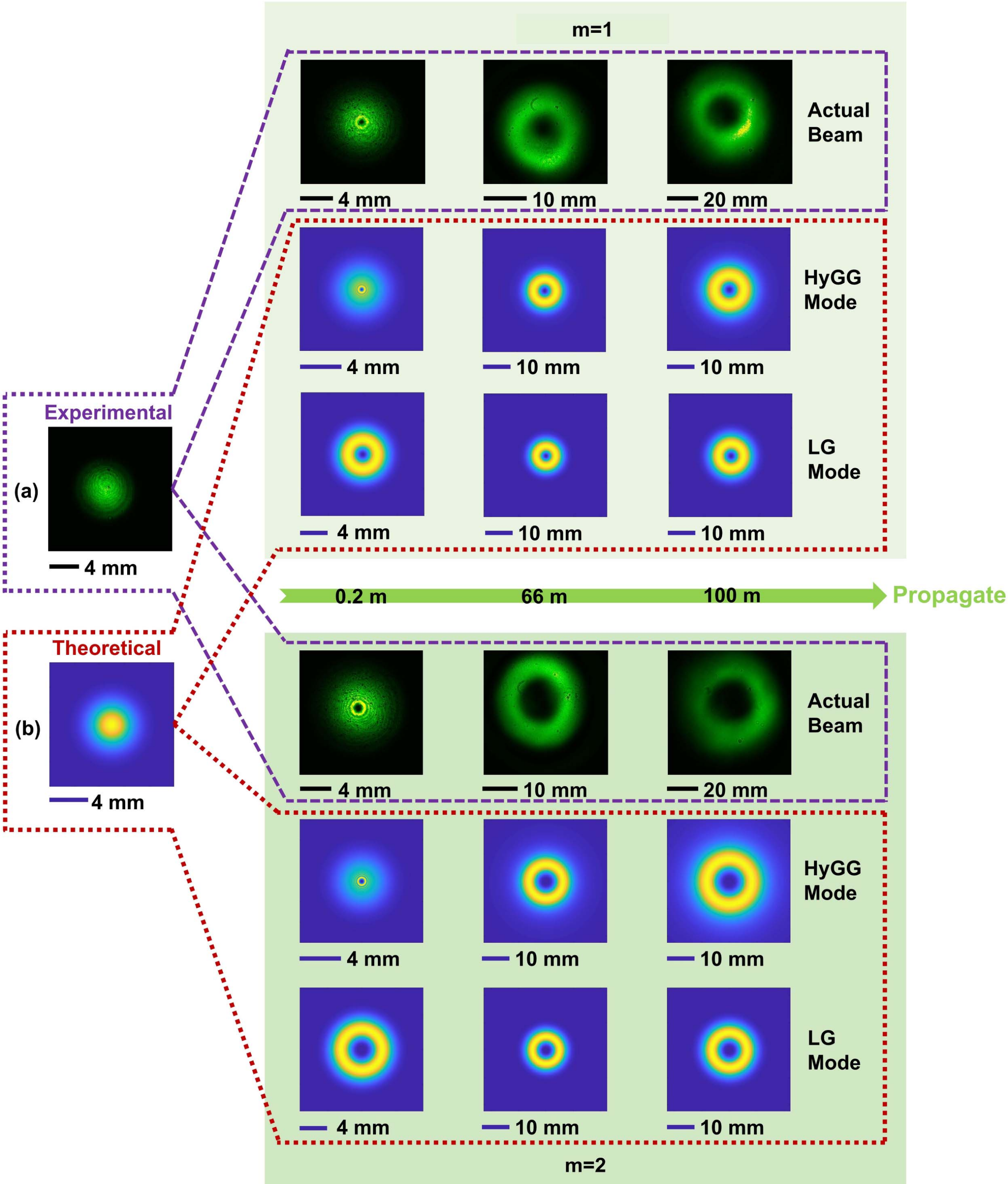

Fig. 2. Categorization of the beam in the experiments. (a) Experimental measurements of vortex beam profiles at different locations along propagation. (b) Theoretical profiles of vortex beams in HyGG mode and LG mode at corresponding locations.

B. Quantifying Turbulence and Effects of PSDs

To optically quantify the turbulence strength and effects in terms of C_n^2, we leverage its relationship with the angle of arrival (AoA). A commonly adopted approach for this estimation assumes a plane wave propagation model and a Kolmogorov turbulence spectrum, under which the relationship between C_n^2 and the variance of the AoA is given by

$$C_n^2 = \sigma^2 (2R_0)^{1/3}/(2.91L), \tag{3}$$

where σ is the variance of the AoA, L is the length of the turbulent region, and R_0 is the initial spot size of the beam [45–48]. This equation is based on Kolmogorov PSD, which omits the effects of the inner and outer scales [49]. In real-world applications, however, the outer scale of turbulence is often constrained by the physical dimensions of the propagation environment, such as obstructions from laboratory equipment and optics, or terrain variations and obstacles in outdoor remote sensing scenarios. Under such conditions, the assumption of an infinite outer scale is no longer valid, and an alternative definition of the power spectral density (PSD) that incorporates a finite outer scale should be adopted. To investigate turbulence strength under different PSD models, we start by modifying Eq. (3) as

$$C_n^2 = A(l_0, L_0, R_0)\sigma^2(2R_0)^{1/3}/(2.91L). \tag{4}$$

Here, we introduce a parameter A, which is determined by the PSD, the inner scale l_0, the outer scale L_0, and the radius of the beam R_0 (see Appendix A for the derivation of the relationship between C_n^2 and σ^2). In addition to the Kolmogorov PSD, of which the mathematical expression is given in Eq. (5), we consider three other PSDs to take inner and outer scales into consideration: Tatarskii PSD, mvK PSD, and modified PSD [49]. The mathematical expressions for these PSDs are given in Eqs. (6)–(8), respectively.

$$\Phi_{\text{Kolmogorov}} = 0.033C_n^2\kappa^{-11/3}, \tag{5}$$

where $\kappa = |2\pi(f_x\hat{x} + f_y\hat{y})|$ is the spatial wavenumber of which the definition is the same in the following equations and f_x and f_y are the x- and y-direction spatial frequencies.

$$\Phi_{\text{Tatarskii}} = 0.033C_n^2\kappa^{-11/3}\exp(-\kappa^2/\kappa_m^2), \tag{6}$$

where $\kappa_m = 5.92/l_0$ and l_0 is the inner scale of the turbulence.

$$\Phi_{\text{mvK}} = 0.033C_n^2\frac{\exp(-\kappa^2/\kappa_m^2)}{(\kappa^2+\kappa_0^2)^{11/6}}, \tag{7}$$

where $\kappa_0 = 2\pi/L_0$, L_0 is the outer scale of the turbulence, and κ_m has the same definition as in Eq. (6). The mvK PSD can be regarded as an enhanced version of the Kolmogorov and Tatarskii spectra, incorporating a Gaussian-shaped truncation at high spatial frequencies to better reflect the physical limitations of real-world turbulence. The mvK PSD permits spatial frequencies to extend from zero to infinity, while progressively suppressing high-frequency components through a smooth, physically realistic decay. These three PSDs have been widely applied in the numerical modeling of turbulence, especially the Kolmogorov and mvK PSDs [30–41]. However, it is worth noting that they do not predict the behavior with high accuracy under certain conditions. For example, the rise in the turbulence PSD near $1/l_0$ that is expected based on the temperature analysis in Refs. [50,51] is not predicted by any of these three PSDs. To overcome this limitation, we adopted a modified atmospheric PSD or, in short, a modified PSD, which is determined by a hydrodynamic analysis followed by an analytical fit [52,53],

$$\Phi_{\text{modified}} = 0.033C_n^2\left[1 + 1.802\left(\frac{\kappa}{\kappa_l}\right) - 0.254\left(\frac{\kappa}{\kappa_l}\right)^{7/6}\right] \times \left[1 - \exp\left(-\frac{\kappa^2}{\kappa_0^2}\right)\right]\frac{\exp(-\kappa^2/\kappa_l^2)}{\kappa^{11/3}}, \tag{8}$$

where $\kappa_l = 3.3/l_0$, $\kappa_0 = C_0/L_0$, and the scaling constant C_0 here can be chosen from 2π, 4π, or 8π, depending on the specific application of the PSD [46]. In this work, C_0 is set to be 8π empirically. Although the modified PSD offers improved theoretical accuracy compared with other aforementioned PSDs, its application has been reported in only a limited number of studies due to its mathematical complexity [54]. In addition, its prediction error and modeling accuracy have not yet been systematically evaluated or compared to other PSDs through experimental validation.

In order to experimentally assess and validate modeling accuracy to address this existing gap, we conducted a set of experiments to quantitatively assess the performance of different PSD models. First, we measured C_n^2 produced by the turbulence generator based on AoA fluctuations using different PSD formulations utilizing a setup shown in Fig. 3(a), and the measurement results are presented in Fig. 3(b). The free-space propagation after the turbulence generator was introduced to increase the centroid deviation and enable reliable AoA detection, under the assumption that its effect is secondary compared to the turbulence-induced phase distortions. However, at very high turbulence strength, the phase profiles of the beams at the exit of the turbulence generator become strongly spatially decorrelated such that their wavefronts can no longer be characterized by a single global tilt but rather multiple local phase gradients. During subsequent propagation, the contributions from these local phase gradients to the beam centroid can partially cancel each other. As a result, the global beam tilt inferred from centroid measurements at the beam profiler may underestimate the intrinsic AoA fluctuations at the generator exit, and the measurement at 50°C may slightly underestimate the variance of the AoA. Therefore, we determine the C_n^2 values at 50°C based on the power-law fitting results shown in Fig. 3(b) to avoid potential bias introduced under strong turbulence conditions, while maintaining consistency with the overall trend observed in the lower turbulence regime. The parameter A in Eq. (4) is also included in the measured and fitted results of C_n^2, of which the determining parameters are set to be $l_0 = 1$ mm, $L_0 = 0.105$ m, and $R_0 = 1.45$ mm. L_0 is provided by the manufacturer of the turbulence generator, and it is constrained by the size of the chamber. R_0 is directly measured at the exit of laser. For the validation of l_0, we measured the structure function D_θ [setup shown in Fig. 3(c)] through the phase profile of the beam with the temperature difference between the air inside and outside the turbulence generator set to 50°C:

$$D_\theta(\rho) = \langle[\theta(\rho_0+\rho) - \theta(\rho_0)]^2\rangle, \tag{9}$$

where θ is the phase of the beam at a certain location and ρ is the distance between two arbitrary points on the transverse plane. Meanwhile, D_θ can also be expressed as

$$D_\theta(\rho) = 8\pi^2k^2L\int_0^\infty \kappa\Phi_n(\kappa)[1 - J_0(\rho\kappa)]\mathrm{d}\kappa, \tag{10}$$

where κ is the spatial frequency, k is the optical wavenumber, L is the length of the turbulent region, which is 0.15 m in our case, $\Phi_n(\kappa)$ is the PSD, and $J_0(x)$ is the zeroth order of the Bessel function of the first kind [55]. Therefore, with the beam expander shown in Fig. 3(c), $D_\theta(\rho)$ can be fitted as a function of ρ to validate the parameters in the PSD over a broader range. The fitting outcome is shown in Fig. 3(d), in which we set $\Phi_n(\kappa)$ to be the expression of the modified PSD as an example.

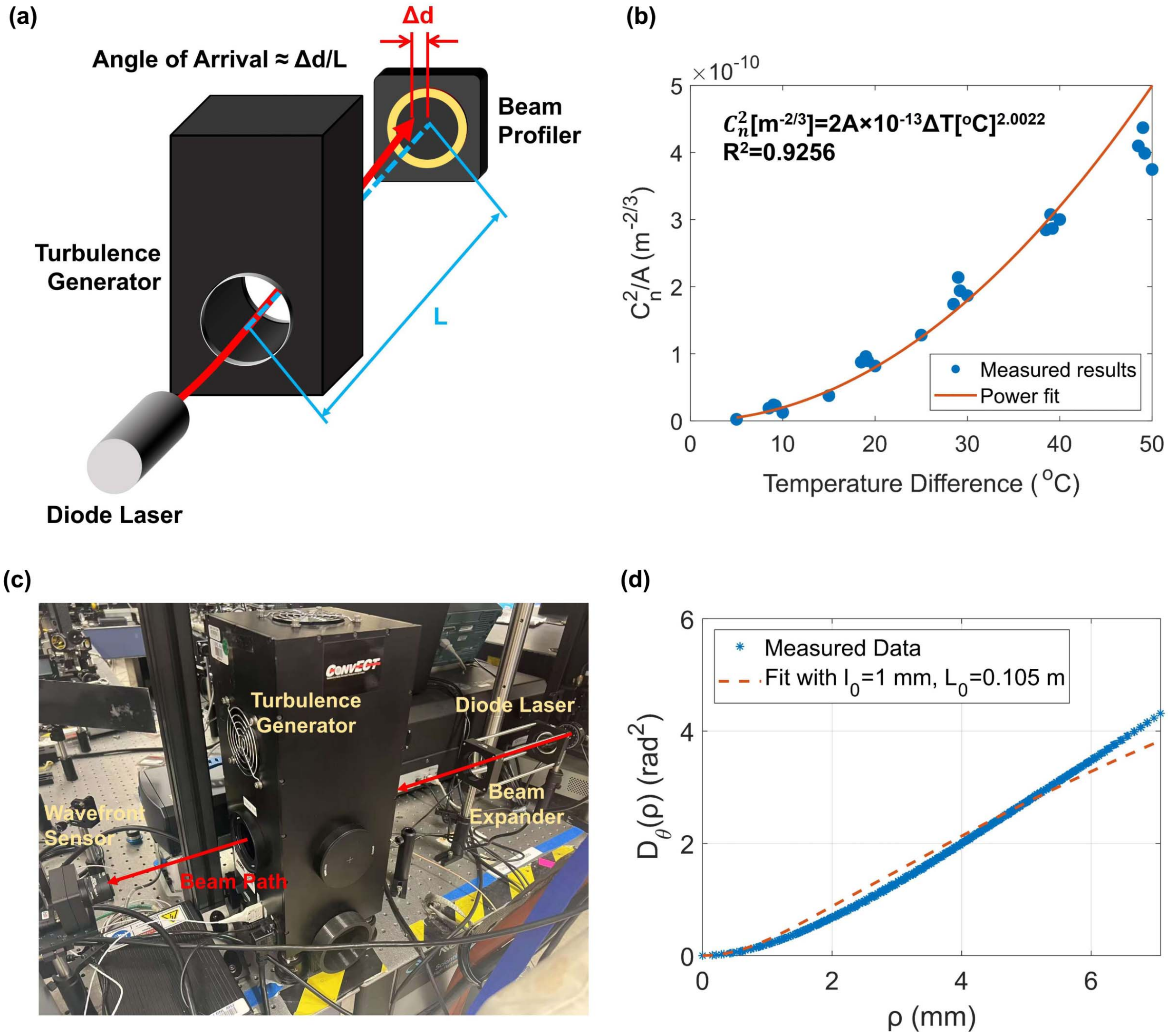

Fig. 3. Measurement of C_n^2 and l_0. (a) Experimental setup to measure the C_n^2. (b) Fitted curve for the relationship between the temperature difference between the air inside and outside the turbulence generator box and the C_n^2. (c) Experimental setup to validate the determination of scale lengths through measurement of the structure function. (d) Fit of the structure function against the spatial separation between two points of the beam with $L_0 = 0.105$ m and $l_0 = 1$ mm.

It reveals that $L_0 = 0.105$ m and $l_0 = 1$ mm yield a good fit for the experimentally measured structure functions. The minor discrepancy at larger values of ρ arises from the reduced intensity near the outer boundary of the Gaussian beam, which increases the influence of ambient noise.

The relation between σ^2 and C_n^2 is presented in Fig. 4(a) for different PSDs. Values of A in Eq. (4) are calculated to be 1.202 for the Tatarskii PSD, 2.067 for the mvK PSD, 2.129 for the modified PSD, and 1 for the Kolmogorov PSD (see Appendix A for detailed calculation procedures). That is, the measured C_n^2 can differ by more than twofold depending on the PSD we adopt. To quantitatively evaluate the prediction performance against experimental observations using different PSD models, we employed the ellipticity and eccentricity as an effective and practical probe by comparing the experimentally measured and numerically predicted ellipticity and eccentricity of vortex beams with different topological charges under turbulence. The ellipticity of a beam at propagation distance z is defined as

$$\xi(z) = \frac{d_{\sigma m}}{d_{\sigma M}}, \tag{11}$$

where $d_{\sigma m}$ is the minor (smaller) beam axis and $d_{\sigma M}$ is the major (larger) beam axis. An ellipticity closer to 1 denotes a more circular beam. Similarly, the eccentricity is defined as

$$e(z) = \sqrt{1 - \xi^2(z)}. \tag{12}$$

An eccentricity closer to zero denotes a more circular beam. In these definitions, the beam width refers to the second-moment width [56]. These two metrics derived from the second-moment methodology provide distinct advantages for evaluating both beam quality and the predictive accuracy of PSD models from two aspects. First, they are inherently more

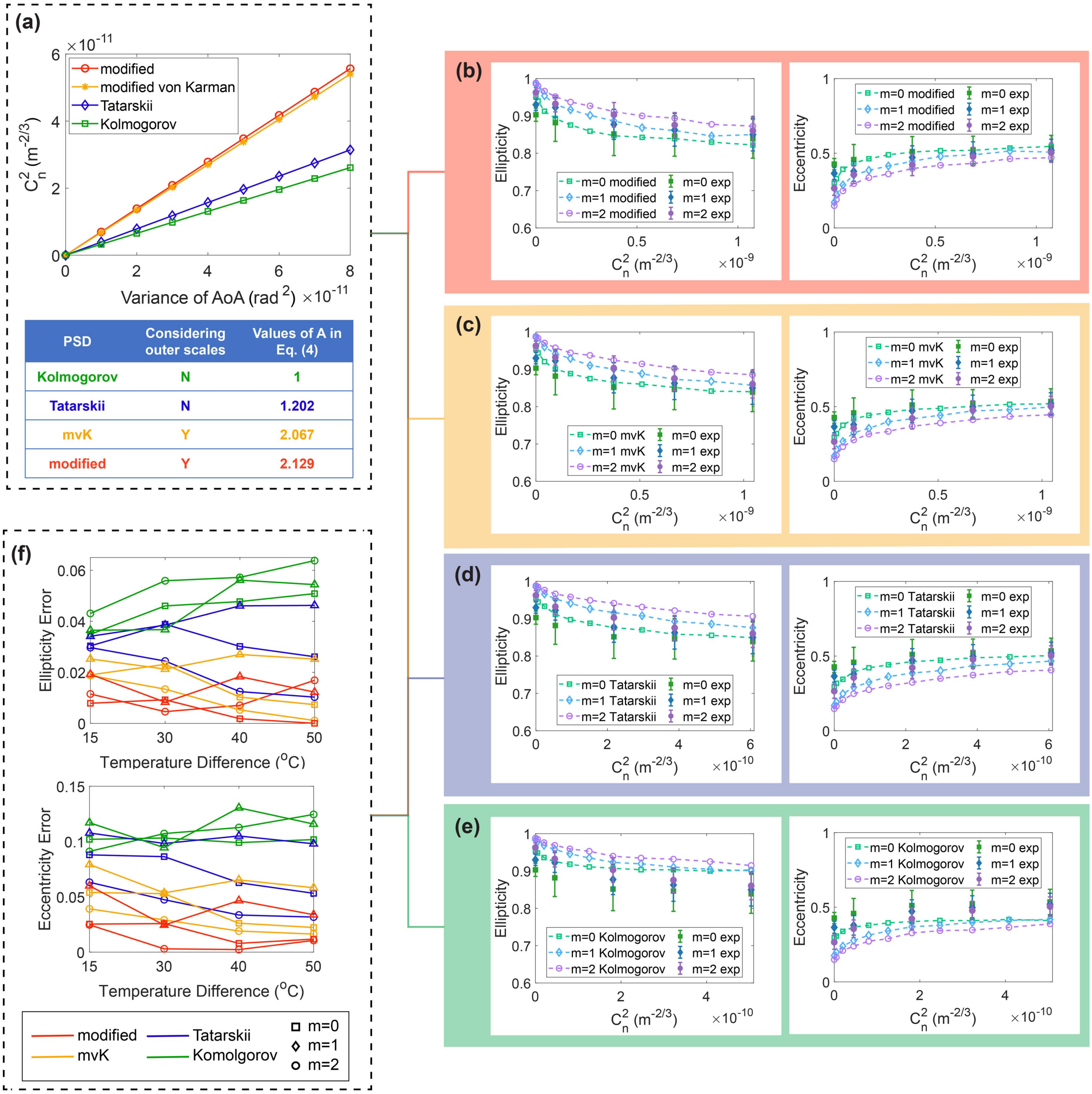

Fig. 4. Comparison between experimentally observed and numerically predicted circularities. (a) C_n^2 versus the variance of AoA for different PSDs and the corresponding comparison between numerical and experimental results for (b) modified, (c) mvK, (d) Tatarskii, and (e) Kolmogorov PSDs. The errors between the numerical and experimental results for different PSDs are summarized in (f). Error bars in panels (b)–(e) stand for standard deviations.

sensitive to intensity distortions, as they incorporate information from the full spatial intensity distribution rather than relying on an intensity-threshold-based boundary. This enables them to capture subtle asymmetries arising from turbulence-induced phase perturbations after diffraction, while also reducing errors associated with illumination-induced artifacts near the boundary of the collecting aperture. Second, the second-moment formulation naturally follows the beam's orientation by quantifying the longest and shortest beam widths along the principal axes. As a result, it effectively tracks and compensates for beam rotation induced by turbulence.

Experimentally, we captured beam profiles of the Gaussian and vortex beams with the setup in Fig. 1(a) at 100 m under ambient turbulence as well as four turbulence strengths produced by the turbulence generator. For each type of beam and each turbulence strength, we obtained 1000 frames. Numerically, we conducted 500 realizations of the propagation simulation for each type of beam, each PSD, and each turbulence strength. The simulation workflow, specific setup parameters, and computational procedures are described in detail in Appendix A. The outcomes of comparative analyses across different PSD models are presented in Figs. 4(b)–4(e),

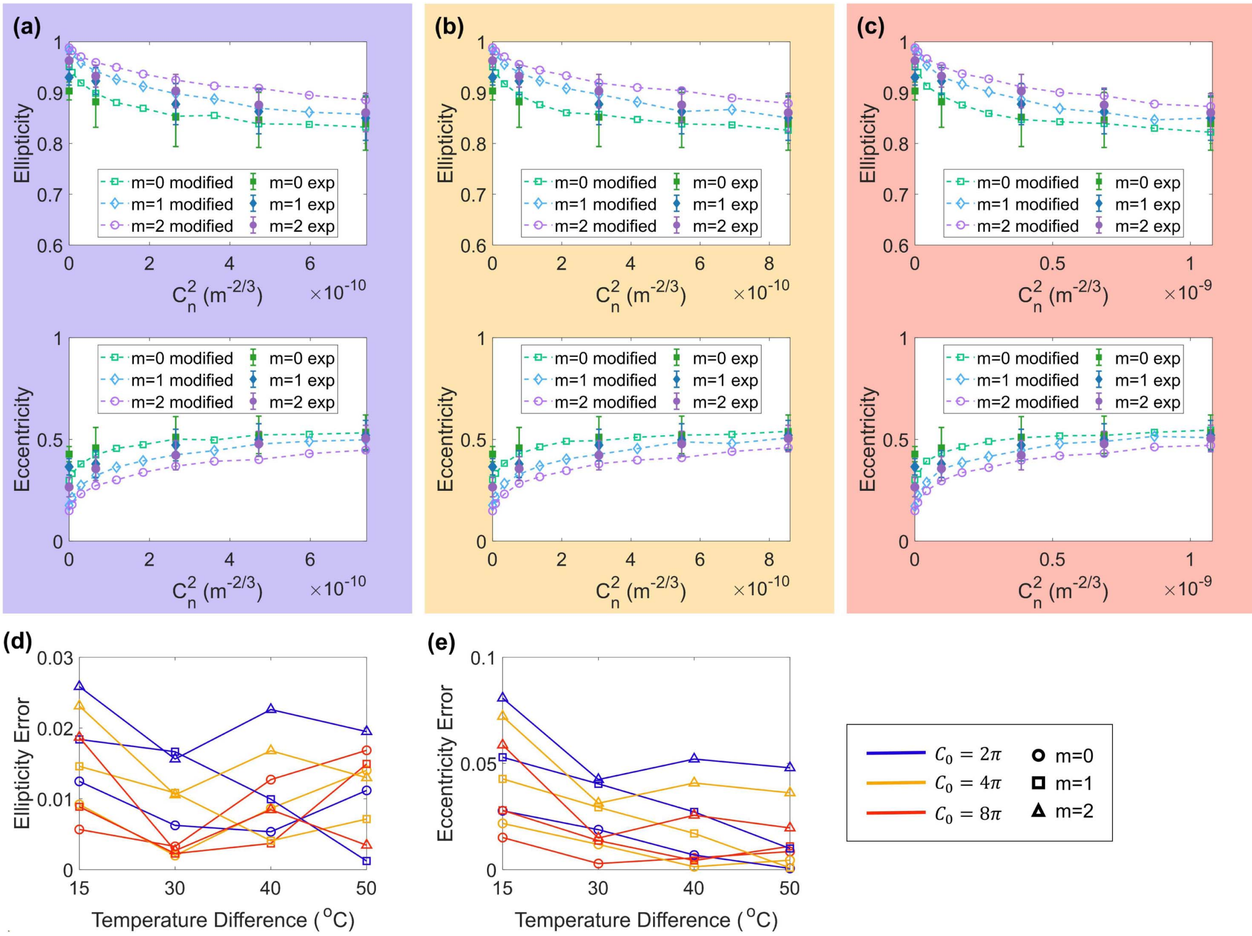

Fig. 5. Comparison of prediction errors in circularity for different choices of the scaling constant in the modified PSD. (a)–(c) Comparison between experimental and simulation results for (a) $C_0 = 2\pi$; (b) $C_0 = 4\pi$; (c) $C_0 = 8\pi$. (d), (e) Corresponding prediction errors in (d) ellipticity and (e) eccentricity. Error bars in panels (a)–(c) stand for standard deviations.

highlighting their varying predictive accuracies under identical turbulence conditions.

The discrepancies between the experimental results and simulation results are summarized in Fig. 4(f) for different turbulence strengths. As different PSDs yield different C_n^2 values, the turbulence strength in this panel is represented by the temperature difference between the air inside and outside the turbulence generator. The prediction errors presented in this panel are defined as the absolute differences between the experimentally measured and numerically simulated values of beam ellipticity and eccentricity. Data corresponding to the condition with the turbulence generator off are excluded from Fig. 4(f), as the ambient turbulence level is too low to render non-Kolmogorov perturbations negligible, such as phase distortions from the surfaces of mirrors. We notice that the application of the modified PSD significantly decreases the errors in Fig. 4(f) compared to other PSDs. When averaged across all topological charges and turbulence strengths with the turbulence generator on, the prediction errors of ellipticity are 0.0098, 0.0164, 0.0306, and 0.0486 for the modified, mvK, Tatarskii, and Kolmogorov PSDs, respectively. For eccentricity, the corresponding average errors are 0.0230, 0.0429, 0.0729, and 0.1083. These results demonstrate that other commonly used PSDs enlarge predictive error by 167% to 496% relative to the modified PSD, or in other words, the modified PSD reduces prediction error up to 79.8%. Meanwhile, Fig. 5 presents a comparison between the two alternative choices of the scaling constant C_0, namely 2π and 4π, and the empirically selected value $C_0 = 8\pi$. Figures 5(a)–5(c) compare the numerically predicted and experimentally measured results, while Figs. 5(d) and 5(e) summarize the prediction errors in ellipticity and eccentricity, respectively, following the same procedure used in Figs. 4(b)–4(f). The results show that both $C_0 = 2\pi$ and 4π lead to larger prediction errors than $C_0 = 8\pi$. Nevertheless, their errors remain smaller than those obtained using the other three PSD models. Specifically, the average ellipticity errors are 0.0112 and 0.0138, and the average eccentricity errors are 0.0258 and 0.0340 for $C_0 = 4\pi$ and 2π, respectively. These numbers in prediction errors support our empirical choice of $C_0 = 8\pi$ and also further demonstrate that the modified PSD leads to improved accuracy of numerical simulations.

These observations underscore the importance of selecting the appropriate PSD for turbulence modeling. First, PSDs that neglect the outer scale systematically underestimate the

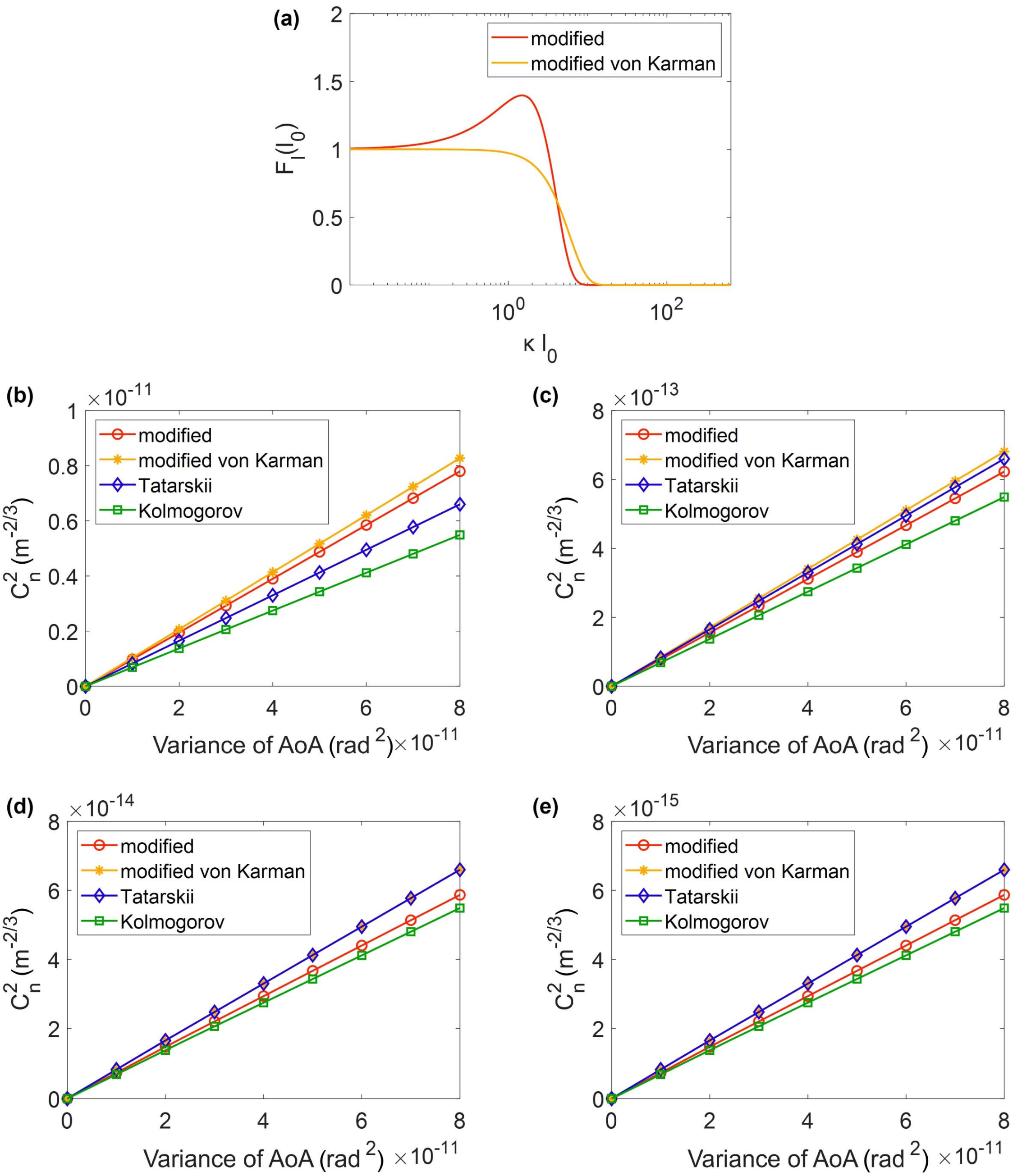

Fig. 6. Difference among PSDs. (a) Inner scale dependence of mvK and modified PSDs. (b)–(e) C_n^2 versus the variance of AoA with the outer scale being (b) 0.5 m, (c) 5 m, (d) 50 m, and (e) 500 m.

effective turbulence strength, which explains the markedly larger prediction errors for the Kolmogorov and Tatarskii PSDs relative to those for the mvK and modified PSDs. Second, further improvement from the mvK PSD to the modified PSD can be attributed to an increased spectral density introduced by the increase of PSD around $\kappa l_0 \approx 1$, which is predicted exclusively by the modified PSD. More specifically, we separate the inner scale related terms in Eqs. (7) and (8) such that the mvK PSD includes the term

$$F_l(l_0) = \exp\left(-\frac{\kappa^2}{\kappa_m^2}\right), \tag{13}$$

while the modified PSD adopts the term

$$F_l(l_0) = \exp\left(-\frac{\kappa^2}{\kappa_l^2}\right)\left[1 + 1.802\left(\frac{\kappa}{\kappa_l}\right) - 0.254\left(\frac{\kappa}{\kappa_l}\right)^{\frac{7}{6}}\right]. \tag{14}$$

As shown in Fig. 6(a), when we plot these terms against the normalized spatial frequency κl_0, both models exhibit nearly identical spectral behavior across the majority of the frequency domain except near $\kappa l_0 \approx 1$. Therefore, the observed difference in prediction accuracy between the mvK and modified PSDs cannot be attributed to differences in parameterization but

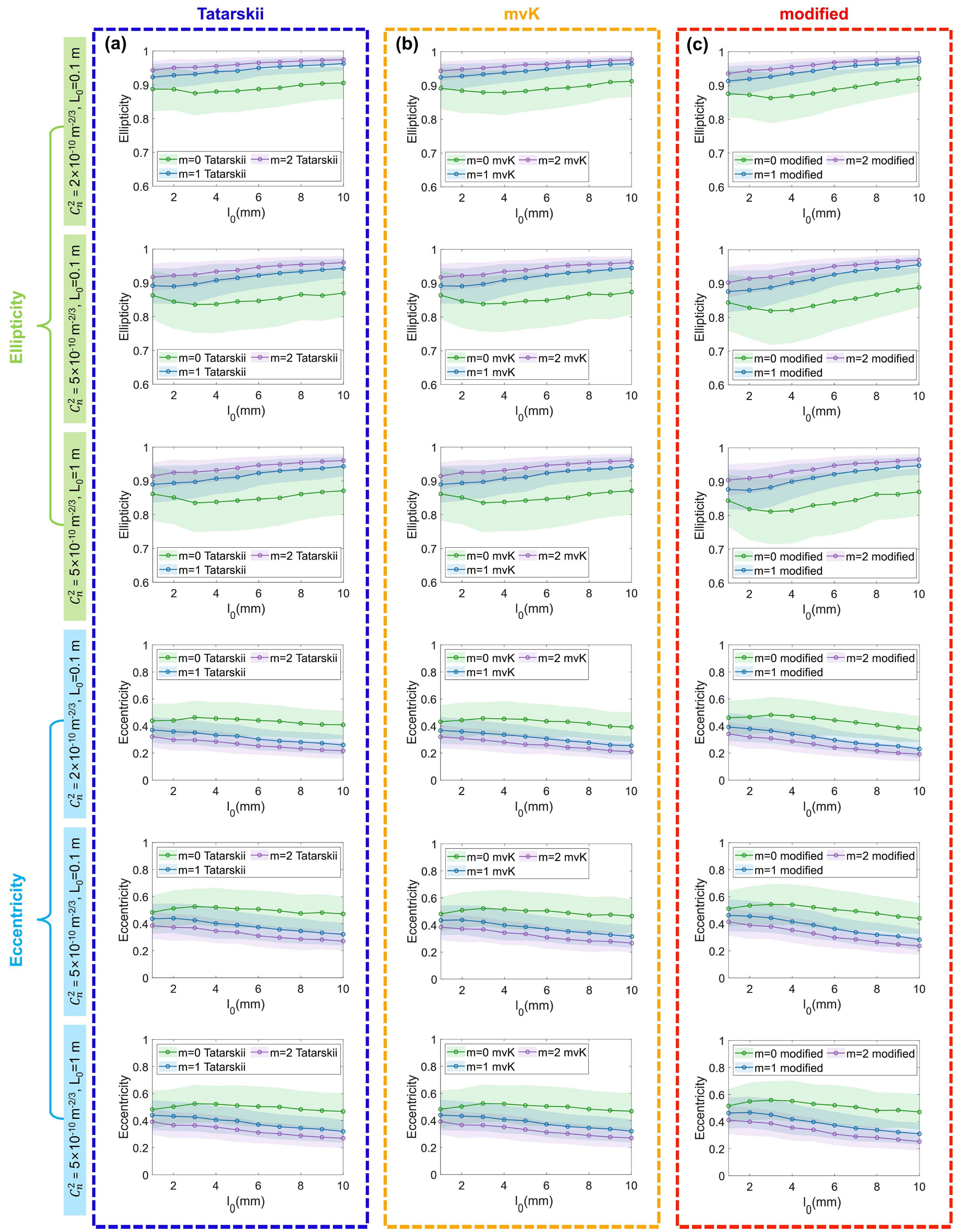

Fig. 7. Beam circularity versus scale lengths. Beam circularity with respect to the inner scales predicted by (a) Tatarskii, (b) mvK, and (c) modified PSDs under three turbulence conditions: $C_n^2 = 2\times10^{-10}\ \mathrm{m}^{-2/3}$ with $L_0 = 0.1$ m, $C_n^2 = 5\times10^{-10}\ \mathrm{m}^{-2/3}$ with $L_0 = 0.1$ m, and $C_n^2 = 5\times10^{-10}\ \mathrm{m}^{-2/3}$ with $L_0 = 1$ m. Shaded regions stand for standard deviations.

rather the localized deviation, namely the bump near $\kappa l_0 \approx 1$ in the modified PSD. This feature leads to higher variance in the frequency domain and, consequently, a greater degree of turbulence-induced stochasticity. As a result, the predicted circularity is further suppressed, producing ellipticity and eccentricity values that align more closely with the experimental observations. Accordingly, we adopt the modified PSD with $C_0 = 8\pi$ for all subsequent calculations of the refractive index structure parameter C_n^2, which reaches a maximum of $1.07 \times 10^{-9}\ \mathrm{m}^{-2/3}$ at a temperature difference of 50°C between the air inside and outside the turbulence generator.

Despite the discrepancies among different PSD models in calculating C_n^2, it should also be noted that these differences gradually diminish as the outer scale increases. The theoretical relationship between C_n^2 and AoA is shown in Figs. 6(b)–6(e). In these analytical calculations, we set the laser diameter to be 2.9 mm and the turbulent region length to be $L = L_0/0.7$ since, in scenarios such as the beam passing through a turbulence generator, it is not physically meaningful for the outer scale to exceed the physical dimensions of the generator. The results suggest that, when the outer scale exceeds several meters, this relationship becomes nearly identical across all models, which is consistent with theoretical expectations.

Beyond the predictive inaccuracy, another limitation of the Kolmogorov PSD is its lack of dependence on characteristic turbulence scales. In contrast, Tatarskii, mvK, and modified PSDs incorporate physical parameters such as kinematic viscosity via inner scale, making them more suitable for characterizing realistic turbulence conditions [46]. Since the impact of turbulence on beam circularity has not been systematically reported before, we further investigated the role of the inner scale in shaping ellipticity and eccentricity. Simulations were performed across varying inner scales, turbulence strengths, and outer scale values. The results for all topological charges $m = 0$, 1, and 2, as well as for Tatarskii, mvK, and modified PSDs, are shown in Fig. 7, with the shaded regions denoting standard deviations. For Gaussian beams, the circularity does not exhibit a strictly monotonic relationship with the inner scale, reflecting two competing mechanisms. First, smaller inner scales are associated with higher energy dissipation rates and stronger perturbations, so the beams show generally improved circularity at relatively larger inner scales. However, when the inner scale is much smaller than the beam diameter, the aperture-averaging effect becomes dominant. As the beam diameter-to-inner scale ratio increases, this effect smooths out turbulence-induced fluctuations and improves beam circularity through the spatial averaging inherent in second-moment-based definitions [57–59]. In contrast, vortex beams exhibit distinct responses due to their different spatial structures and sizes. For most scenarios, their circularity increased monotonically with the inner scale, except for a certain case of $m = 1$, where the inner scale is much smaller than the beam width. Additionally, we compare the influence of different outer scales and find that their variation had a negligible impact on beam circularity metrics, which aligns with previous findings in Ref. [59]. Nevertheless, it does not imply that the outer scale effects are negligible. As a matter of fact, given the nearly identical results predicted by the Tatarskii and mvK PSDs under the same turbulence strength, it is the neglect of the outer scale in Tatarskii PSD that leads to an underestimation of turbulence strength and consequently larger prediction errors, as shown in Fig. 4.

These findings are highly relevant to both real-world applications and laboratory investigations of atmospheric turbulence, as physical structures, terrains, obstacles, and optical equipments may constrain the outer scale through their spatial dimensions. For example, in our experiments, the outer scale within the turbulence generator could not exceed the length of one side of the generator box. Moreover, the implications extend to simulated turbulence, particularly those generated with the Fresnel scaling method [60–63], which applies phase screens closely tied to the choice of PSD. Our results offer insights into how PSD selection affects the reliability and accuracy of in-lab turbulence simulation in such contexts.

C. Vortex Beam as a Resilient Mode for Atmospheric Propagation

1. Ellipticity, Eccentricity, and Degradation

Building upon the results above, we established a well-characterized turbulence platform that enables further experimental evaluation of the performance advantages of vortex beams. First of all, the HyGG mode exhibits a clear advantage in preserving beam circularity under turbulence [Figs. 4(b)–4(e)]. Notably, this is a rather unique advantage for the HyGG mode, while other modes, such as LG modes, do not necessarily possess this property [64]. This preserved circularity is associated with practical benefits in applications involving the delivery of optical energy through atmospheric turbulence. For example, it can result in reduced sensitivity to misalignment, along with more consistent and potentially higher coupling efficiency in FSO systems, given a sufficiently large aperture. In LiDAR applications, it can also reduce measurement bias and improve the consistency of the backscattered signal.

To further explore the advantages of HyGG modes, we present histograms of ellipticity and eccentricity at varying turbulence strengths in Figs. 8(a) and 8(b). The normal distributions revealed by the histograms statistically justify the comparison of mean and standard deviation in this work. Additionally, histograms broaden as C_n^2 increases, while a higher topological charge number reduces the broadening effect, indicating enhanced resistance to turbulence-induced beam distortions. These differences in broadening behavior across topological charges can be attributed to the self-healing property of optical vortices. Phase singularity, as a central feature of the helical wavefront, has been shown to reconstruct in subsequent propagation after severe perturbations, and the resulting redistribution of energy through diffraction preserves the intensity profile and vortex structure [65,66]. In turbulent conditions, this topological constraint improves the structural robustness of vortex beams and leads to more compact measurement results by limiting the extent of phase randomization and enhancing the resilience to spatial coherence loss. According to previous analytical analysis, one indicator of the degree of coherence is turbulence-induced degradation, which means vortex beams gradually evolve toward Gaussian-like intensity profiles in atmospheric propagation [19]. Moreover, vortex beams with higher topological charges require longer propagation distance or stronger turbulence to undergo such a transformation. To demonstrate this evolution for the HyGG modes experimentally, we extract the cross-sectional intensity profiles across the beam centroid, as shown in Figs. 8(c) and 8(d), for HyGG modes with $m = 1$ and $m = 2$ under three different turbulence strengths. For illustrative clarity and noise suppression, 10 consecutive frames are

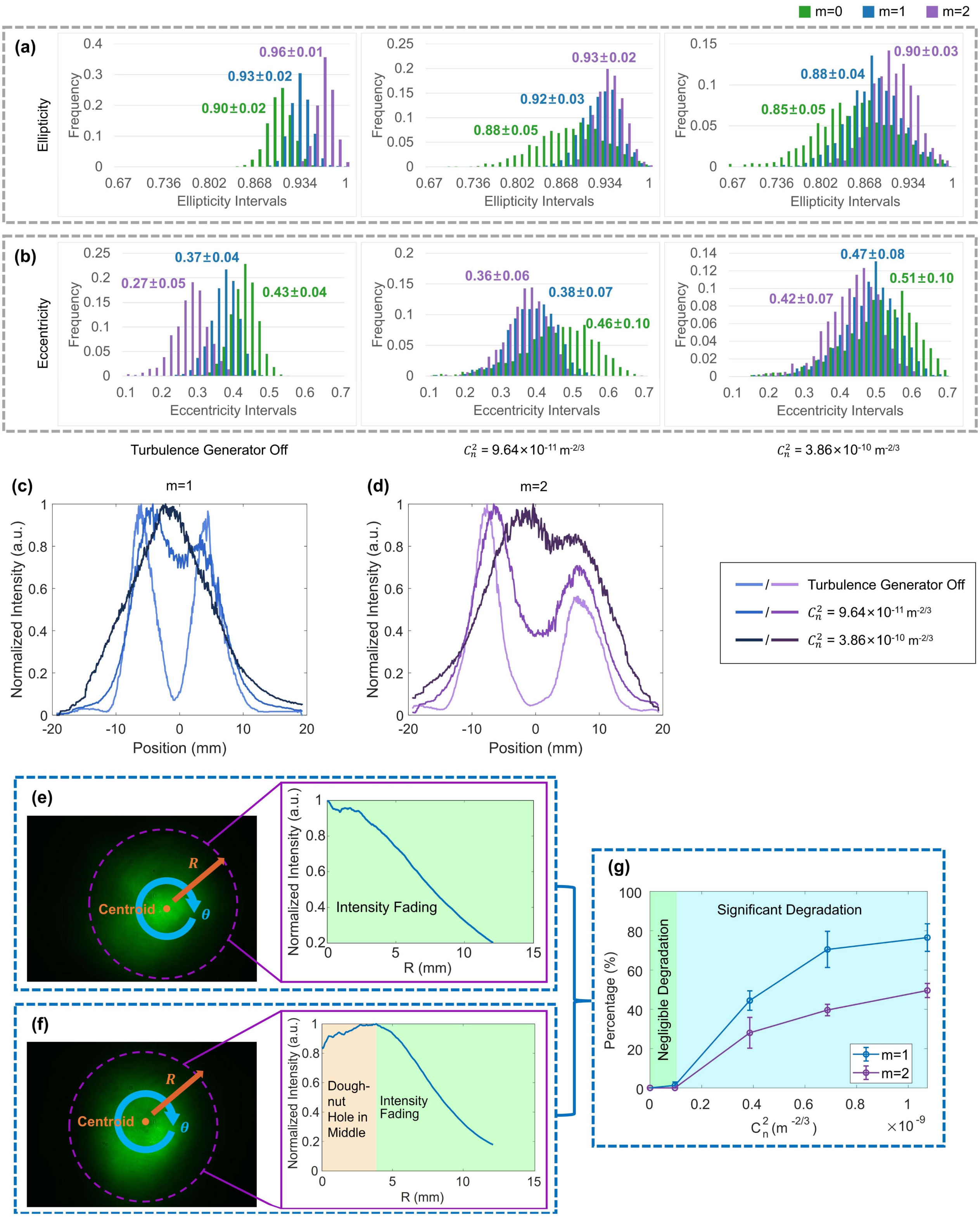

Fig. 8. Advantages of vortex beams in preserving structural properties in turbulence. (a), (b) Histograms of (a) ellipticity and (b) eccentricity of the fundamental Gaussian beam ($m = 0$) and HyGG vortex beams ($m = 1, 2$) under three different turbulence levels. Each histogram is labeled with the corresponding mean and standard deviation. (c), (d) Normalized cross-sectional intensity profiles of HyGG vortex beams with (c) $m = 1$ and (d) $m = 2$ captured at 100 m under different turbulence strengths. (e), (f) Examples of the radial distribution of normalized azimuthal average intensity for a degraded and non-degraded vortex beam. An $m = 1$ vortex beam at $C_n^2 = 3.86 \times 10^{-10}\ \mathrm{m}^{-2/3}$ is shown here with (e) vanished doughnut structure and peak average azimuthal intensity is located less than 2% of the beam width away from the centroid; (f) double-peaked structure and peak average azimuthal intensity is located more than 2% of the beam width away from the centroid. (g) Percentages of frames in which the intensity distribution becomes Gaussian for two topological charges $m = 1$ and 2 in different turbulence strengths. Error bars in panel (g) stand for standard deviations.

averaged. As the turbulence strength increases, we observe a noticeable rise in on-axis intensity, indicating a gradual degradation from doughnut-shaped to Gaussian-like profiles.

As reported in Ref. [19], the overall degradation effect can be captured by statistical parameters such as the average intensity profile derived from the coherence length $\rho_0 = (0.545 C_n^2 k^2 z)^{-3/5}$, where k is the wavenumber and z is the propagation distance. However, such analytically averaged quantities do not reflect the inherently stochastic nature of turbulence. In contrast, this randomness can only be revealed through individual observations of a large ensemble of beam profiles. Therefore, in this study, we perform a frame-by-frame analysis of dynamically evolving intensity profiles. When the turbulence generator was off, the vortex beams with non-zero topological charges show very clear double-peak cross-sectional structures in every frame, so the two intensity peaks appear very clear in the lightest-colored curves in both Figs. 8(c) and 8(d). When the turbulence strength reaches $C_n^2 = 9.64 \times 10^{-11}\ \mathrm{m}^{-2/3}$, a double-peak cross-sectional structure is still maintained by the beams with either $m = 1$ or 2 for most of the frames. However, when the turbulence strength reaches $C_n^2 = 3.86 \times 10^{-10}\ \mathrm{m}^{-2/3}$, we observe that, in a certain fraction of frames, the vortex beams degraded into a Gaussian-like profile, which aligns with the stochasticity of turbulence effects. To quantitatively assess the degradation probability across different turbulence strengths and topological charges, we develop a frame-by-frame classification method based on pixel-level numerical analysis. This approach applies a consistent and objective criterion to each frame, avoiding reliance on subjective visual inspection of cross-sectional profiles. The specific procedures are detailed as follows. First, we set the origin of each frame as the intensity-centroid of the beam to define a polar coordinate (R, θ). The intensity-centroid of the beam (x_0, y_0) is defined by equations $x_0 = \frac{\sum xI(x,y)}{\sum I(x,y)}$ and $y_0 = \frac{\sum yI(x,y)}{\sum I(x,y)}$, where (x, y) is the pixel coordinate and $I(x, y)$ is the intensity at that pixel. Then, the average azimuthal intensity is set by $I(R) = \frac{1}{2\pi}\int_0^{2\pi} I(\theta)\mathrm{d}\theta$, and we identify the global maximum as $I(R_0) = \max\{I(R)\}$. If R_0 is less than 2% of the beam width, the intensity distribution is determined to be single-peaked. The typical single-peaked and double-peaked $I(R)$ distributions we retrieve from the frames are presented in Figs. 8(e) and 8(f), respectively. In the experiments, a total of 500 frames of beam profile were recorded and grouped into five sets of 100 frames each for every condition. We compute the percentage of frames in which the intensity distribution is classified as single-peaked, indicating vortex beam degradation. These degradation percentages, shown in Fig. 8(g) for each topological charge, reveal clear trends with respect to turbulence strength and topological charge. At $C_n^2 = 9.64 \times 10^{-11}\ \mathrm{m}^{-2/3}$, the beam with $m = 1$ exhibits degradation in a small portion of frames, while the beam with $m = 2$ still maintains its doughnut structure well. When the turbulence strength increases to $C_n^2 = 3.86 \times 10^{-10}\ \mathrm{m}^{-2/3}$, the vortex beams with both topological charges degrade in a significant percentage of the frames, yet the proportion of degraded frames is markedly higher with $m = 1$. In other words, contrary to prior analytical predictions suggesting that degradation occurs only beyond certain thresholds of propagation distance and turbulence strength, our results demonstrate that vortex beam degradation can still arise even under modest turbulence but with lower probability. In fact, our findings consistently show that vortex beams with higher topological charges exhibit greater resilience, as evidenced by a lower probability of degradation and a higher threshold turbulence strength required for such degradation to become noticeable. These results suggest that higher-order vortex beams exhibit enhanced robustness in turbulent environments, making them more suitable for long-distance free-space applications where coherence preservation is critical.

We also evaluate additional metrics reflecting the spatial intensity distributions for vortex and Gaussian beams under turbulence, as listed in Table 2. Among them, the roughness of the Gaussian fit indicates the similarity between the measured intensity distribution and an ideal Gaussian profile. As shown in Fig. 9(a), for vortex beams, roughness increases with the topological charge but decreases with the turbulence strength, while for Gaussian beams, it increases with the turbulence strength. This trend supports the interpretation and quantification in Fig. 8(g) that turbulence distorts Gaussian beams and degrades vortex beams toward Gaussian profiles, with higher topological charges offering greater resistance to this transformation. For the other three metrics in Table 2, centroid wandering, flatness, and uniformity, no significant trend across different topological charges is observed. However, as shown in Fig. 9(b), when subjected to principal component analysis (PCA) and projected onto the first two principal components, vortex beams with

Table 2. Definitions of Metrics Measured for Vortex Beams Other Than Circularity

Metric	Definition	Variable
Roughness of Gaussian fit	$R = \frac{\lvert E_{ij} - E_{ij}^f \rvert_{\max}}{E_{\max}}$	E_{ij}: energy density distribution at the (i, j) pixel E_{ij}^f: fitted theoretical Gaussian distribution at the (i, j) pixel $E_{\max}$: maximum energy density of the incoming beam
Centroid wandering	$\Delta d_c(z) = \frac{\sum_{i=1}^{N}[(x-\bar{x})^2 + (y-\bar{y})^2]}{N}$	x/y: horizontal/vertical position of the centroid of the beam $\bar{x}/\bar{y}$: average horizontal/vertical position of the centroid of the beam N: number of frames captured
Flatness	$F_\eta(z) = \frac{E_\eta}{E_{\max}}$	E_η: effective average energy density $E_{\max}$: peak energy density in the beam
Uniformity	$U_\eta(z) = \frac{1}{E_\eta}\sqrt{\frac{1}{A_\eta^i}\iint [E(x, y) - E_\eta]^2 \mathrm{d}x\mathrm{d}y}$	A_η^i: area containing the above energy $E(x, y)$: effective average energy density at (x, y)

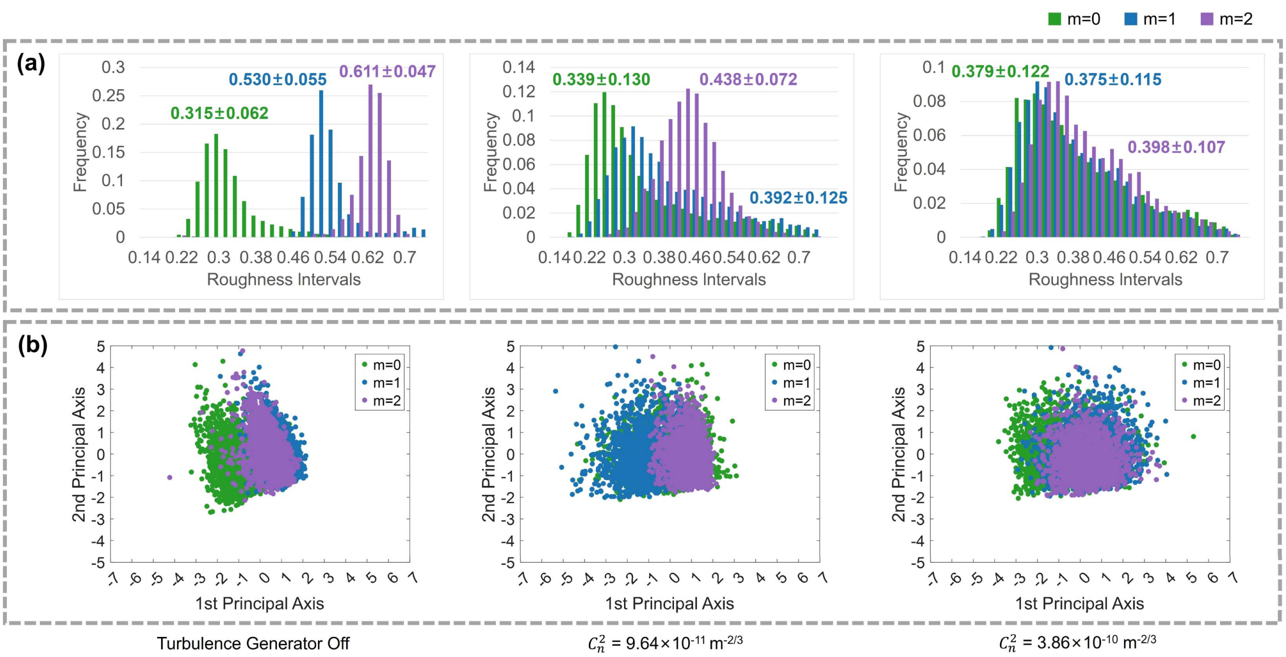

Fig. 9. Measurement results of other quality-assessing metrics for beams with different topological charges. (a) Histograms of the roughness of the Gaussian fit with different topological charges and different turbulence strengths. (b) PCA for centroid wandering, flatness, and uniformity across different topological charges and different turbulence strengths.

higher topological charges exhibit more compact clustering in turbulent conditions. This behavior indicates improved overall stability of beam properties under turbulence.

2. Scintillation Index and Collection Efficiency

Another indicator of the degree of coherence is the scintillation index (SI), which also quantifies intensity fluctuations [17,18]. This connection stems from turbulence-induced phase randomization, which reduces spatial coherence and enhances intensity distortions, thereby leading to higher SI. SI is calculated by the variance of intensity at a given location divided by the square of the ensemble average of intensity as shown in Eq. (15) [17,18],

$$\sigma_I^2 = \frac{\langle I^2 \rangle - \langle I \rangle^2}{\langle I \rangle^2}, \tag{15}$$

where I is the intensity and the angle bracket stands for ensemble average. Prior to measuring SI, we verified the temporal power stability of the laser and the output power along the beam path to ensure that the observed intensity fluctuations originated from turbulence, rather than the laser source. The output power of the laser source over a 10 min interval is shown in Fig. 10(a), with a standard deviation of only 0.25%. Meanwhile, when the turbulence generator is off, the total power measured at different propagation locations for beams with various topological charges is presented in Fig. 10(b). Although power loss occurs due to the non-unity reflectivity of the mirrors and beam divergence during propagation, the measured values remain highly stable even in the presence of ambient turbulence, as evidenced by their small standard deviations. These results indicate that the influence of power fluctuations from the laser itself is negligible and the SI measurements are reliable. It should be noted that the relative ordering of the remaining power percentages among different topological charges is not strictly preserved across propagation distances. This behavior arises from the fact that the remaining power is normalized by different initial powers, as the initial power is measured after the laser exit for the Gaussian beams but after the vortex retarders for vortex beams. Due to slight differences in the transmissivity of vortex retarders for different topological charges, the initial power varies across different beams. As a result, the curves representing different topological charges may intersect or change their relative ordering. However, each curve still exhibits a monotonic decrease with propagation distance, and the remaining percentages remain relatively close across different topological charges.

Then, for each topological charge, we recorded 500 frames in five groups with 100 frames in each group. The corresponding SI is calculated based on Eq. (15). To fairly compare Gaussian and vortex beams, especially given the doughnut-shaped profile of vortex beams, we plug in the global maximum of the azimuthally averaged intensity profile to Eq. (15), ensuring consistency and fairness across different beam types (SI values here cannot be estimated through the Rytov variance due to a different definition of intensity and a strong gradient of turbulence strength at the optical exit of the turbulence generator). As shown in Fig. 11(a), vortex beams consistently exhibit lower SI values than Gaussian beams in the investigated range of turbulence strength, with the SI decreasing further as the topological charge increases. These results support the conclusion that higher-order vortex beams possess greater spatial coherence and better resistance to turbulence-induced intensity fluctuations, making them more suitable for stable power delivery.

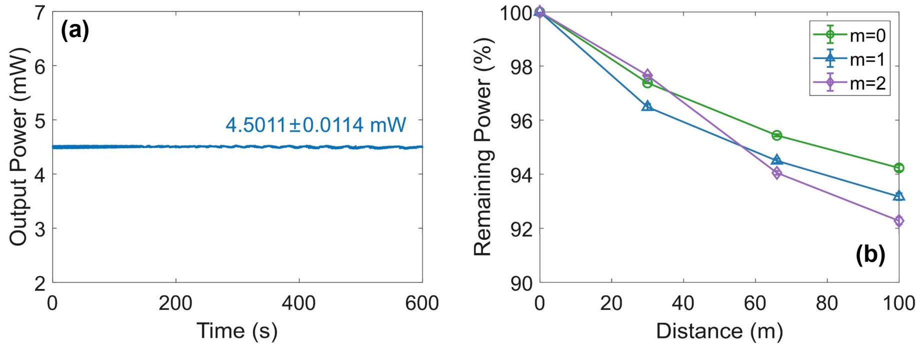

Fig. 10. Verification of laser power stability. (a) Output power of the 532 nm laser source over time. (b) Remaining percentages of beam power measured at different locations with different topological charges. Error bars in panel (b) stand for standard deviations.

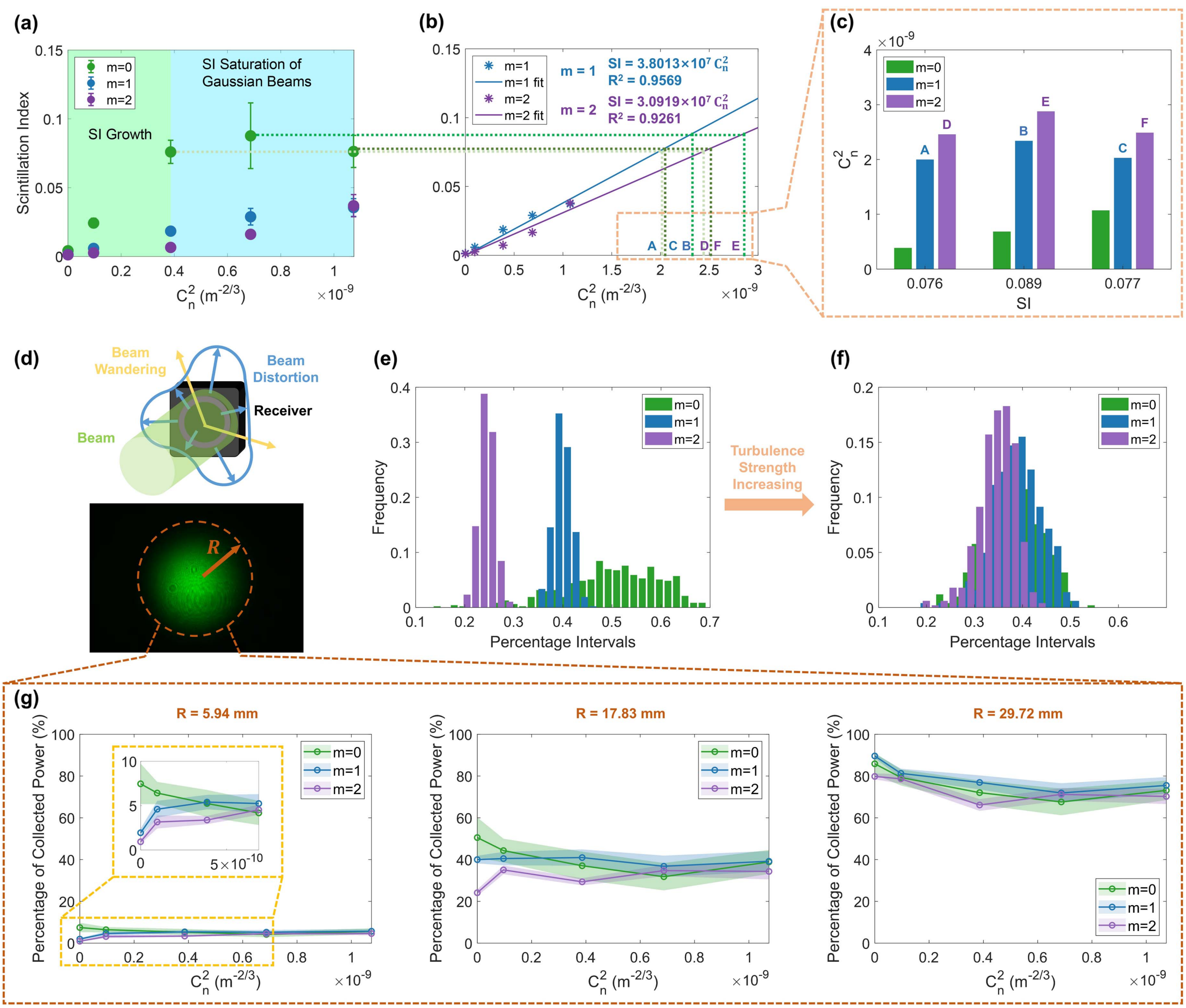

Fig. 11. Fluctuation of intensity and collection efficiency for vortex beams in turbulence. (a) SI for conventional Gaussian beams ($m = 0$) and HyGG vortex beams ($m = 1, 2$) under different turbulence strengths. (b) Fitting to predict the SI values produced by vortex beams at stronger turbulence. (c) Comparison among C_n^2 values at which Gaussian and vortex beams produce about the same SI. (d) Factors leading to compromised collection efficiency (upper) and an illustration of the receiver with limited aperture (lower). (e) Probability distribution of the percentage of power collected by an aperture with a radius of 17.83 mm over 500 frames under turbulence with $C_n^2 = 7.19 \times 10^{-15}\ \mathrm{m}^{-2/3}$. (f) Probability distribution of the percentage of power collected by an aperture with a radius of 17.83 mm over 500 frames under turbulence with $C_n^2 = 1.07 \times 10^{-9}\ \mathrm{m}^{-2/3}$. (g) Effects of the aperture size on the collection efficiency of Gaussian and vortex beams. Error bars in panel (a) and shaded regions in panel (g) stand for standard deviations.

Since the vortex beams finally degrade into Gaussian beams in turbulence, the SI levels of the vortex beams can also be similar to those of Gaussian beams with strong turbulence. This occurs when the SI of the Gaussian beam reaches saturation, consistent with findings in Ref. [17], allowing the SIs of vortex beams to approach similar values. To quantify the relative resilience of vortex beams, we performed a linear fit of SI versus C_n^2 for topological charges $m = 1$ and 2, as shown in Fig. 11(b), to determine the C_n^2 values at which vortex beams reached the same SI as the saturated Gaussian beam. The results are shown in Fig. 11(c), which reveal that vortex beams exhibit substantially greater robustness to turbulence, withstanding turbulence strengths more than 5 times higher than those for Gaussian beams and reaching as high as a 6.37-fold improvement in group D, before yielding comparable SI values. However, this advantage gradually fades away as the turbulence strength increases due to vortex beam degradation and saturation of SI for Gaussian beams. Nevertheless, since the C_n^2 used in our study already corresponds to an exceptionally strong turbulence regime, it is still reasonable to conclude that the reduced intensity fluctuations of vortex beams remain robust across a broad and practically relevant range of turbulent conditions.

To further substantiate the intensity-related advantages of vortex beams, we additionally examined a well-recognized limitation: their collection efficiency. The inherently larger beam size, stronger divergence, and doughnut-shaped intensity profile of vortex beams are often listed together with turbulence as key factors degrading the collection efficiency of OAM-based atmospheric links when the receiver aperture is limited, such as in FSO systems [67]. As shown in Fig. 11(d), when the beam exceeds the aperture and turbulence induces beam wandering or distortion, the collection efficiency, which is defined as the fraction of total power falling within a given aperture [as illustrated by the circumscribed circle in Fig. 11(d)] drops below unity.

Interestingly, our results indicate that turbulence reduces the difference in collection efficiency between Gaussian and vortex beams. For example, with a receiver radius of 17.83 mm, the pronounced trend of decreasing collection efficiency with increasing topological charge when $C_n^2 = 7.19 \times 10^{-15}\ \mathrm{m}^{-2/3}$ [Fig. 11(e)] becomes almost negligible when the strength of turbulence increases to $C_n^2 = 1.07 \times 10^{-9}\ \mathrm{m}^{-2/3}$ [Fig. 11(f)]. This behavior can be interpreted using the other two turbulence-induced features of vortex beams revealed in this study. First, turbulence partially degrades the vortex structure and shifts the maximum power density from the doughnut ring toward the beam center, thereby allowing a larger fraction of energy to fall within the aperture. Second, vortex beams maintain better circularity than Gaussian beams, resulting in a more compact and balanced energy distribution along both transverse directions, which helps compensate for their initially larger size and more severe divergence along propagation. These two facts can also explain why a slight increase in collection efficiency is observed as the turbulence strength increases when the aperture is small [left two plots of Fig. 11(g)]. Furthermore, as compared in the three plots of Fig. 11(g), enlarging the aperture further reduces the differences among topological charges since a larger aperture gradually captures more of the high-intensity doughnut ring of vortex beams. Therefore, despite their larger beam sizes, collection efficiency does not fundamentally limit the applicability of vortex beams. In practical optical systems, it can be readily mitigated through appropriate design of the collection optics, for example, by incorporating beam-reduction optics. What may more fundamentally affect the overall energy efficiency of vortex beams is the loss introduced by the vortex generation hardware. In this work, vortex beams are generated using vortex retarders with a transmission efficiency of approximately 97%, keeping energy loss at a low level. Meanwhile, with the rapid development of vortex beam generation technologies, including spatial light modulators (SLMs) [68,69], metasurfaces [70–74], and on-chip vortex beam generators [75], the advantages of vortex beams are becoming increasingly accessible. These platforms enable flexible generation of multiple vortex modes and topological charges, often within compact or even microscale systems. However, it is important to recognize the trade-off between mode flexibility and energy efficiency in such technologies. For example, phase modulation in most SLMs relies on pixelated liquid crystal panels, where non-unity fill factors introduce diffraction effects, including zeroth- and higher-order diffractions that redistribute optical power into undesired directions and reduce overall energy efficiency [76–78]. These considerations suggest that future developments in vortex beam generation should aim to balance mode versatility with optical efficiency, which will be critical for their effective deployment in practical free-space optical systems.

3. DISCUSSION

This work demonstrates the superior performance of vortex beams in atmospheric turbulence, along with the significant improvement in modeling accuracy achieved through the appropriate selection of power spectral density (PSD) models. At the same time, the results point to several promising directions for future research to further enhance the applicability of vortex beams and the reliability of numerical modeling. First, the observed standard deviations in the beam circularity and scintillation index (SI) suggest a potential limitation of multi-frame numerical simulations. In such simulations, phase screens are independently generated for each realization, whereas in physical experiments, atmospheric parameters such as temperature, and consequently refractive index and phase delay, evolve continuously over time. This temporal continuity is absent in simulations, leading to an overestimation of fluctuations in certain beam characteristics. This effect may plausibly contribute to the systematic overprediction of the standard deviation of circularity observed in Figs. 12(a)–12(d). Since the Kolmogorov and Tatarskii PSD models fail to accurately capture the turbulence strength, which directly affects the predicted standard deviations, comparisons are only presented between the experimentally measured standard deviations and those numerically simulated using the mvK and modified PSDs. In addition, a comparison of Figs. 12(e) and 12(f) with Fig. 11(a) indicates that the numerical simulations also overestimate the SI values for all topological charges under strong turbulence conditions. Due to constraints imposed by the distribution statistics in the spatial frequency domain, the predicted mean values of beam properties remain unchanged. Although discrepancies exist between experimentally measured and numerically predicted

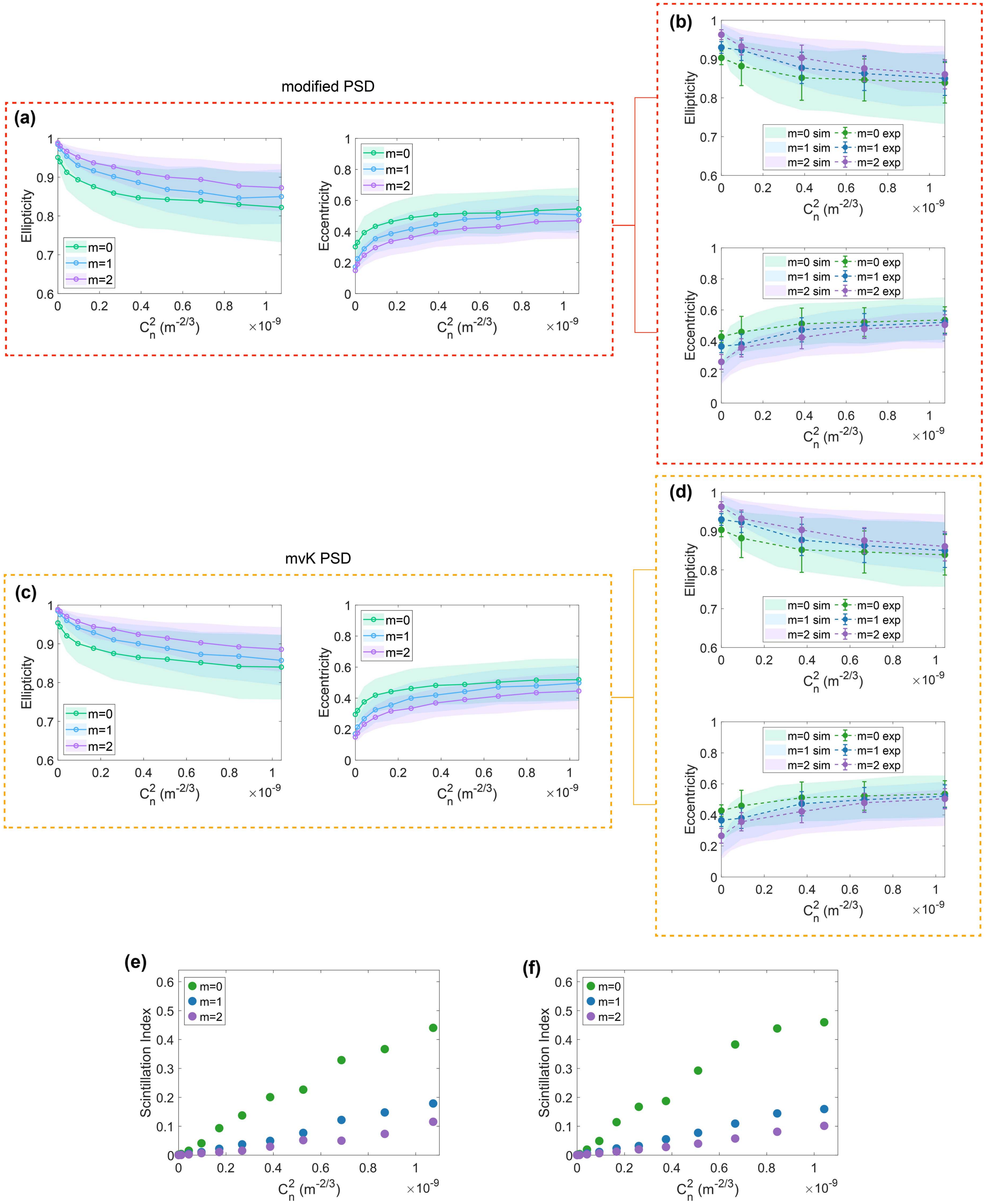

Fig. 12. Comparison between experimentally measured and numerically simulated standard deviations. (a) Beam circularities predicted by modified PSD in numerical simulations with standard deviations and (b) their comparison with experimentally observed standard deviations. (c) Beam circularities predicted by mvK PSD in numerical simulations with standard deviations and (d) their comparison with experimentally observed standard deviations. (e) SI predicted by numerical simulations with modified PSD. (f) SI predicted by numerical simulations with mvK PSD. The shaded regions in panels (a)–(d) represent numerically predicted standard deviations.

SI values, the trend that higher topological charge leads to lower intensity fluctuations remains consistent across both experiments and simulations. As a result, the main conclusions of this study remain unaffected. Nevertheless, the observed overestimation of standard deviations and SI values by numerical simulations provides an important reference for future improvements in phase-screen-based modeling. In particular, investigating temporal correlations and developing models that capture the continuous evolution of turbulence effects, such as spatially shifted phase screens [35] or more generalized analytical approaches, may represent an important next step toward more accurate predictions of fluctuation statistics in atmospheric propagation.

Second, field experiments are still desirable to further validate the results. Although the integrated turbulence strength over propagation distance can be matched between localized strong turbulence generated in the laboratory and distributed weaker natural atmospheric turbulence, this equivalence primarily captures the averaged effects of turbulence on beam properties. However, whether it fully reproduces all detailed statistical characteristics of natural atmospheric turbulence remains to be verified. In addition, direct free-space propagation in field experiments, without the use of folded optical paths involving multiple mirrors, can help reduce unintended wavefront distortions introduced by mirror surface imperfections.

Finally, the integration of robust beam design and accurate turbulence modeling represents a promising direction for improving the performance of next-generation optical systems. In this context, the demonstrated synergy between beam resilience and model fidelity highlights the importance of jointly optimizing physical beam properties and numerical descriptions of turbulence. Looking forward, this synergy can be further enhanced by advances in adaptive optics [79] and machine learning [80]. Compared with the current experimental setup, these approaches offer significant potential for real-time correction and dynamic adaptation to varying turbulence conditions, thereby further mitigating turbulence-induced distortions and enabling more robust performance in complex and time-varying environments.

4. CONCLUSION

In this study, we combined simulations and experiments to demonstrate that vortex beams outperform conventional Gaussian beams in long-range atmospheric propagation, especially under strong turbulence. This superiority, manifested in reduced intensity fluctuations and improved structural resilience, becomes more pronounced with increasing topological charge. Specifically, vortex beams in the HyGG mode exhibit enhanced robustness, not only in maintaining beam coherence but also in preserving beam circularity, which is one of the key properties for ensuring reliable remote optical performance in turbulent environments.

Crucially, we also show that an appropriate choice of a refractive index PSD model based on the propagation environment, especially the outer scale, has a substantial impact on both turbulence strength estimation and numerical prediction accuracy. When the outer scale of turbulence is small, as commonly encountered in spatially constrained or engineered flow environments, PSDs that neglect the outer scale can underestimate the refractive index structure parameter C_n^2 by up to 50%, leading to significant mischaracterization of propagation conditions. In contrast, switching to the modified PSD can reduce beam circularity prediction error by up to 79.8%, establishing a clear advantage in both model fidelity and simulation reliability.

In conclusion, HyGG vortex beams with higher topological charges provide superior shape preservation and turbulence resistance, making them strong candidates for advanced free-space optical communication and remote sensing systems. Our findings highlight the necessity of appropriate turbulence model selection for accurate system design, environmental adaptation, and the development of resilient optical technologies in real-world propagation environments.

APPENIDX A: METHODS

1. Experiment

Setup. Due to limitations of the indoor lab space, the 100 m beam path was implemented in a folded path using five mirrors, as shown in Fig. 1(a). A continuous wave diode laser (Thorlabs CPS532) with a wavelength of 532 nm and a $1/e^2$ beam diameter of 3.5 mm served as the light source of the experiments. The diameter of the beam was adjusted to 6 mm by the beam expander. The vortex beams with non-zero topological charges were converted from conventional Gaussian beams with the vortex retarders of the corresponding order. With the retarders of the corresponding order being flipped up and down, the topological charge of the beam can be switched among 0 (a fundamental Gaussian beam), 1, and 2. Since the polarization state of the vortex beams does not affect their intensity profiles in atmospheric propagation [19], we leave the polarization state of the beam source as partially polarized with a polarization extinction ratio (PER) of 4 dB to preserve power. Moreover, if we collect the reflected signal from a target in remote sensing with vortex beams, such imperfect polarization helps reduce the fluctuation of intensity caused by different polarization reflectivities of the target [81]. Since the orientations of the fast axes of the vortex retarders vary with respect to the azimuthal angle, the output polarization state of the vortex beams is a cylindrical vector after the vortex retarders. The choice of a cylindrical vector beam (CVB) was motivated by the finding that the OAM state spreads less into adjacent states in turbulence for a CVB than a linearly polarized beam [82]. Furthermore, HyGG modes form an overcomplete and non-orthogonal basis, but reliable encoding and decoding remain feasible because of the polarization singularity of the CVB. As a result, the advantages of HyGG modes in maintaining beam quality and circularity during atmospheric propagation can still be effectively leveraged in such polarization states in optical communication systems [83]. The red rectangle on the beam path in Fig. 1(a) indicates the location where turbulence was injected into the beam path. To create stable, controllable, and repeatable turbulence effects, we introduced the convective eddy compact turbulence generator (MZA ConvECT) as shown in the inset in Fig. 1(a). This turbulence generator works by mixing room temperature and heated air, resulting in fully developed turbulent flow conditions. When light passes through the optical ports of the turbulence generator, the phase profile is affected by the spatially varying refractive index of the air medium within the chamber. The generated turbulence is controlled by the temperature difference between the ambient temperature and the temperature of the mixed air inside the generator, which is set by the controller unit, where a larger temperature difference results in stronger turbulence conditions. In each operation, sufficient time was provided for the hot air flow to fully warm up or to reach a new set value, allowing the temperature field and the associated refractive index fluctuations to stabilize. This ensured that the generated turbulence maintained consistent strength during the measurement process. At the end of the 100 m propagation, the beams were captured by a CCD camera-based beam profiler (Newport LBP2-HR-VIS2). To fully capture the beams and ensure that the entire beam went into the aperture of the beam profiler, a focal lens with an aperture diameter of 4 inch and a focal length of 300 mm was placed in front of the beam profiler. Overall, this experimental setup was built to simulate a real-world remote sensing scenario in which a highly turbulent region restricts the optical access to a remote target, so the laser beams were launched to pass through a highly turbulent region with a subsequent long optical path in ambient air.

Calculating C_n^2 from the Variance of the AoA. In this study, C_n^2 is calculated from the variance of the AoA in the following process. First, we express the structure function as shown in Eq. (10). Here we assume a plane wave when the beam passes through the turbulence generator since the laser source has a small divergence angle of 0.6 mrad. In the meantime, the difference in the phase retardance between two points on the wavefront creates a tilting effect that can be expressed as

$$\sigma^2 = D_\theta(\rho)/(k\rho)^2, \tag{A1}$$

where σ^2 is the variance of the AoA [47]. By taking ρ as the diameter of the laser such that $\rho = 2R_0$, we can relate C_n^2 directly to σ^2, and this relationship depends on the selection of $\Phi_n(\kappa)$. This gives us the form of Eq. (4), which means now C_n^2 can be calculated from the variance of AoA and we have the parameter A depending on the choice of PSD. More specifically, C_n^2 can be separated from the expressions of PSDs as

$$\Phi_n(\kappa) = C_n^2\Phi_0(\kappa). \tag{A2}$$

Then Eq. (10) can be written as

$$D_\theta(2R_0) = 8\pi^2k^2LC_n^2\int_0^\infty \kappa\Phi_0(\kappa)[1 - J_0(2R_0\kappa)]\mathrm{d}\kappa. \tag{A3}$$

Substituting Eq. (A3) into Eq. (A1) yields

$$C_n^2 = \sigma^2(2R_0)^2/\left\{8\pi^2L\int_0^\infty \kappa\Phi_0(\kappa)[1 - J_0(2R_0\kappa)]\mathrm{d}\kappa\right\}. \tag{A4}$$

Plugging Eq. (A4) into Eq. (4) gives

$$A(l_0, L_0, R_0) = 2.91(2R_0)^{5/3}/\left\{8\pi^2\int_0^\infty \kappa\Phi_0(\kappa)[1 - J_0(2R_0\kappa)]\mathrm{d}\kappa\right\}. \tag{A5}$$

For the Kolmogorov PSD, Eq. (A5) can be evaluated analytically due to its simple power-law form. For other PSD models, however, the coefficient A must be determined numerically. It is worth noting that a singularity appears in Tatarskii PSD at $\kappa = 0$. In practice, this singularity is effectively suppressed because $1 - J_0(0) = 0$, which cancels the divergence at the origin. For the modified PSD, the limit of $\kappa\Phi_0(\kappa)[1 - J_0(2R_0\kappa)]$ approaches zero as $\kappa \to 0$, rendering the singularity noncontributive to the integral.

Comparison of C_n^2 and l_0 Values to a Real-Life Scenario. The inner scale can be theoretically calculated as $l_0 = 7.4(\nu^3/\varepsilon)^{1/4}$, where ν is the kinematic viscosity of air and ε is the dissipation rate of kinetic energy per unit mass [46]. In the turbulence generator, ν can vary from $1.56 \times 10^{-5}\ \mathrm{m^2/s}$ to $2.14 \times 10^{-5}\ \mathrm{m^2/s}$ from 25°C to 75°C. For the range of ε, recall that the strength of turbulence provided by the turbulence generator is at the level of the air at the jet engine exhaust [20–22]; therefore, we can apply the models described in Refs. [84,85] for the kinetic energy dissipation rate against time after the wake vortex of an aircraft engine. For example, for a Boeing-747 with a lateral span of 50 m and an initial vortex descent velocity of 1.8 m/s, the resulting energy dissipation rates are $38.67\ \mathrm{m^2/s^3}$ and $11.46\ \mathrm{m^2/s^3}$ at 3 and 4.5 s after the wake vortex is injected, respectively (note that, in the reference publication, non-dimensional time and the energy dissipation rate were used, but here they are converted to dimensional values). Therefore, ε is estimated to be from $10\ \mathrm{m^2/s^3}$ to $30\ \mathrm{m^2/s^3}$, and consequently the resulting inner scale is calculated to be about 1 mm. This is also consistent with previous studies in Ref. [21], where the analysis was performed at a similar level of turbulence strength.

Meanwhile, several beam properties, such as log-amplitude variance [86], averaged intensity distribution, and polarization state [19], depend analytically on the integral of C_n^2 over the propagation distance. Consequently, owing to the very high turbulence strength within the generator, the induced turbulence effects can be equivalently interpreted in terms of a weaker turbulence distributed over a much longer propagation distance. For example, the relatively localized turbulence with $C_n^2 = 1 \times 10^{-9}\ \mathrm{m^{-2/3}}$ over a distance of 0.15 m yields a comparable integrated turbulence strength to a weaker turbulence with $C_n^2 = 1 \times 10^{-13}\ \mathrm{m^{-2/3}}$ over a distance of 1.5 km.

In this work, for measurements conducted with the turbulence generator activated, the flow corresponds to a regime of very strong turbulence with a substantially high kinetic energy dissipation rate. Therefore, a constant inner scale is assumed across the four temperature differences. However, for experiments performed under significantly weaker turbulence conditions with lower temperature differences, this fixed inner-scale assumption may no longer be valid and would require recalibration following the procedure described for Fig. 3. As for the outer scale, since it is primarily determined by the physical dimensions of the turbulence generator, it should be re-evaluated when different experimental configurations or physical conditions are applied.

2. Simulation

We applied the Rayleigh–Sommerfeld method [87,88] to model the optical propagation over 100 m with the turbulence generator placed at the start of the beam path. The schematic diagram of the simulation setup and the workflow of the

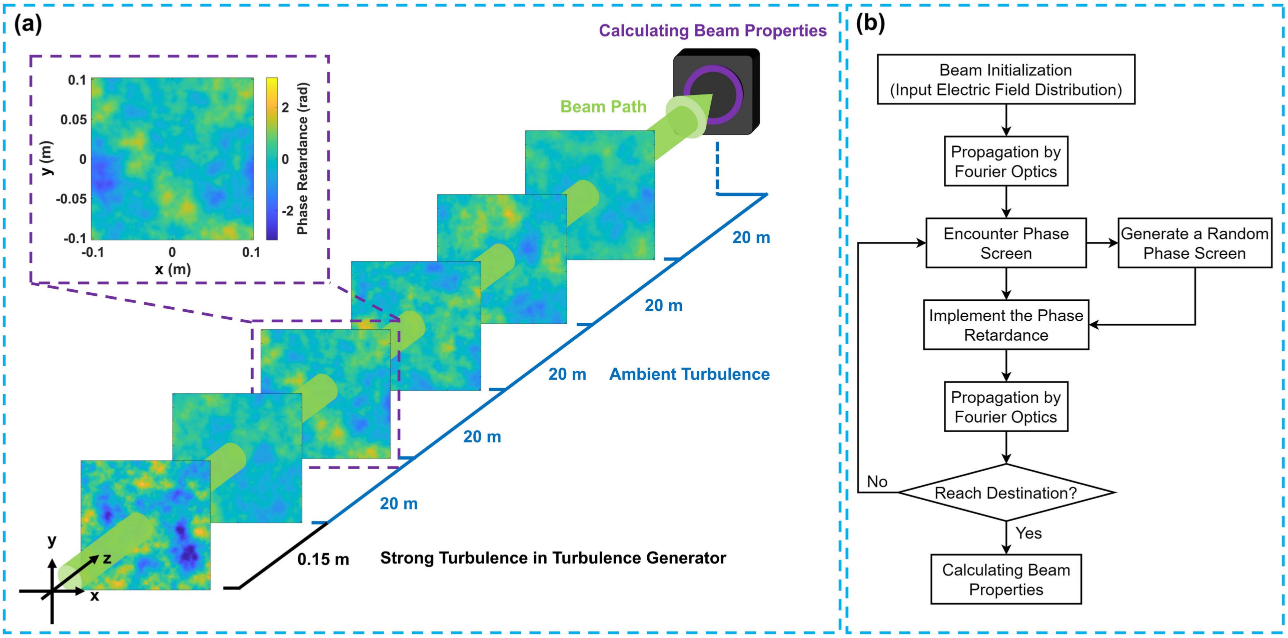

Fig. 13. Setup of numerical simulation. (a) Schematic diagram and (b) logistic flow of the simulation. The inset panel in (a) shows an example of the phase screen with the false color representing the phase retardance.

simulation process are shown in Figs. 13(a) and 13(b), respectively. The propagation of light from one plane to another was calculated by the angular spectrum methods, which can be mathematically expressed as follows:

$$U(x,y,z+\Delta z) = \mathcal{F}^{-1}\{\mathcal{F}[U(x,y,z)\phi(x,y)](\xi,\eta)e^{ik_z\Delta z}\}(x,y), \tag{A6}$$

where $U(x,y,z)$ and $U(x,y,z+\Delta z)$ are the complex electric fields on the transverse plane at z and $z+\Delta z$ in the propagation direction, $\mathcal{F}$ and $\mathcal{F}^{-1}$ denote the Fourier and inverse Fourier transforms, respectively, $(\xi,\eta) = (\frac{1}{x_i}, \frac{1}{y_i})$ are the spatial frequencies in the transverse directions, k_z is given by $k_z = 2\pi\sqrt{(\frac{1}{\lambda})^2 - \xi^2 - \eta^2}$, λ is the wavelength, and $\phi(x,y)$ is the phase screen that simulates the turbulence effect. The optical phase of the generated phase screen can be written as

$$\phi(x,y) = \sum_{n=-\infty}^{\infty}\sum_{m=-\infty}^{\infty} c_{m,n}\exp[i2\pi(f_{x_n}x + f_{y_m}y)], \tag{A7}$$

where f_{x_n} and f_{y_m} are the discrete x- and y-direction spatial frequencies and $c_{m,n}$ denotes the corresponding Fourier-series coefficient. According to the central limit theorem, $c_{m,n}$ follows a normal distribution, as the phase variations induced by atmospheric turbulence arise from a large number of independent random inhomogeneities along the optical path. In general, $c_{m,n}$ are complex-valued, with both the real and imaginary components having zero means, equal variances, and mutually zero cross-covariance. Consequently, the coefficients obey circular complex Gaussian statistics with zero mean, with their variance being expressed as

$$\langle|c_{m,n}|^2\rangle = \Phi_{\mathrm{PSD}}(f_{x_n}, f_{y_m})\Delta f_{x_n}\Delta f_{y_m}, \tag{A8}$$

where Φ_{PSD} is the PSD of which the expressions are given in Eqs. (5)–(8), and Δf_{x_n} and Δf_{y_m} are the frequency spacings that are the inverse of the x and y grid sizes, respectively [86,89,90].

The turbulence generator was represented by one phase screen, and the laser beam propagation in ambient air was simulated by five equally spaced screens over a 100 m distance. Every phase screen in the simulation is constructed on a numerical grid with 2048 × 2048 nodes and a grid spacing of 100 μm. To implement the corresponding turbulence strength into the phase screens, C_n^2 was converted to the Fried parameter r_0 for each screen. Depending on the wavefront, the Fried parameter can be related to C_n^2 through the following expressions:

$$r_{0,\mathrm{pw}} = \left(0.423k^2\sum_i C_{n_i}^2\Delta z_i\right)^{-3/5} = \left(\sum_i r_{0_i}^{-5/3}\right)^{-3/5}, \tag{A9}$$

$$r_{0,\mathrm{sw}} = \left[0.423k^2\sum_i C_{n_i}^2\left(\frac{z_i}{\Delta z}\right)^{5/3}\Delta z_i\right]^{-3/5} = \left[\sum_i r_{0_i}^{-5/3}\left(\frac{z_i}{\Delta z}\right)^{5/3}\Delta z_i\right]^{-3/5}, \tag{A10}$$

where pw and sw denote plane wave and spherical wave, respectively. k is the wavenumber, $C_{n_i}^2$ denotes the refractive index structure parameter represented by the ith screen, r_{0_i} denotes the Fried parameter of the ith screen, z_i is the location of the ith screen in the propagation direction, Δz_i is the distance between the ith screen to the next, and Δz is the total propagation distance. For the phase screen emulating the turbulence generator, since a plane wave and a single-screen configuration are assumed, the Fried parameter on this screen can be calculated as $r_0 = (0.423k^2 C_n^2 \Delta z)^{-3/5}$, in which case $\Delta z = 0.15$ m. It is worth mentioning that, for PSDs other than Kolmogorov PSD, this expression remains valid only when the term of $0.033C_n^2$ in the PSD definitions given by Eqs. (5)–(8) is replaced with $0.49r_0^{-5/3}$ in the numerical implementation; otherwise, the constant 0.423 needs to be recalculated.

For multiple phase screens, we introduce the relationship between r_0 and log-amplitude variances to form an equation set. Similarly, this relationship also depends on the type of wavefront:

$$\sigma^2_{\chi,\mathrm{pw}} = 1.33k^{-5/6}\Delta z^{5/6}\sum_i r_{0_i}^{-5/3}\left(1-\frac{z_i}{\Delta z}\right)^{5/6}, \tag{A11}$$

$$\sigma^2_{\chi,\mathrm{sw}} = 1.33k^{-5/6}\Delta z^{5/6}\sum_i r_{0_i}^{-5/3}\left(\frac{z_i}{\Delta z}\right)^{5/6}\left(1-\frac{z_i}{\Delta z}\right)^{5/6}. \tag{A12}$$

In this way, the values of r_{0_i} can be computed through constrained optimization with the locations of phase screens fixed to reduce the number of unknowns [86]. For a plane wave, the final equation set can be written in a matrix form as

$$\begin{bmatrix} r_{0,\mathrm{pw}}^{-5/3} \\ \frac{\sigma^2_{\chi,\mathrm{pw}}}{1.33k^{-5/6}\Delta z^{5/6}} \end{bmatrix} = \begin{bmatrix} 1 & \cdots & 1 \\ \left(1-\frac{z_1}{\Delta z}\right)^{5/6} & \cdots & \left(1-\frac{z_n}{\Delta z}\right)^{5/6} \end{bmatrix} \begin{bmatrix} r_{0,1}^{-5/3} \\ \vdots \\ r_{0,n}^{-5/3} \end{bmatrix}, \tag{A13}$$

where n is the total number of phase screens. For a spherical wave, of which the wavefront more closely resembles that of beams propagating over extended distances, such as the 100 m propagation in ambient turbulence considered in this study, the matrix form becomes

$$\begin{bmatrix} r_{0,\mathrm{sw}}^{-5/3} \\ \frac{\sigma^2_{\chi,\mathrm{sw}}}{1.33k^{-5/6}\Delta z^{5/6}} \end{bmatrix} = \begin{bmatrix} \left(\frac{z_1}{\Delta z}\right)^{5/3} & \cdots & \left(\frac{z_n}{\Delta z}\right)^{5/3} \\ \left(\frac{z_1}{\Delta z}\right)^{5/6}\left(1-\frac{z_1}{\Delta z}\right)^{5/6} & \cdots & \left(\frac{z_n}{\Delta z}\right)^{5/6}\left(1-\frac{z_n}{\Delta z}\right)^{5/6} \end{bmatrix} \begin{bmatrix} r_{0,1}^{-5/3} \\ \vdots \\ r_{0,n}^{-5/3} \end{bmatrix}. \tag{A14}$$

In Eqs. (A11)–(A14), it is worth noting that the factors $(1-\frac{z_i}{\Delta z})^{5/6}$ and $(\frac{z_i}{\Delta z})^{5/6}(1-\frac{z_i}{\Delta z})^{5/6}$ are essential for the multilayer phase screen configuration. These weighting terms ensure that phase screens located at different positions contribute nonuniformly to the overall wavefront distortion, reflecting the fact that turbulence encountered earlier in the propagation has a different impact compared to turbulence closer to the observation plane. As a result, the cumulative beam degradation along the 100 m propagation in ambient turbulence is accurately reproduced through the weighted superposition of the five phase screens. This subsequent propagation is critical for generating detectable and statistically meaningful beam distortion and scintillation following the localized strong turbulence introduced by the turbulence generator.

Funding. United States Department of Energy, National Nuclear Security Administration, Office of Defense Nuclear Nonproliferation (DE-AC02-05CH11231).

Author Contributions. Conceptualization: VZ, BZ, WL, CK. Methodology: BZ, CK, WL, JC, XM, RH, VZ. Investigation: BZ, CK, WL. Visualization: BZ. Supervision: VZ. Writing—original draft: BZ. Writing—review & editing: BZ, CK, WL, JC, XM, RH, VZ.

Disclosures. The authors declare no conflicts of interest.

Data Availability. Data and codes underlying the results presented in this paper are available in Ref. [91].

REFERENCES

1. K. Zhao, J. C. Suarez, M. Garcia, *et al.*, "Utility of multitemporal lidar for forest and carbon monitoring: tree growth, biomass dynamics, and carbon flux," Remote Sens. Environ. **204**, 883–897 (2018).
2. H. Xu, E. M. Toman, K. Zhao, *et al.*, "Fusion of lidar and aerial imagery to map wetlands and channels via deep convolutional neural network," Transp. Res. Rec. **2676**, 374–381 (2022).
3. S. Maurice, S. M. Clegg, R. C. Wiens, *et al.*, "ChemCam activities and discoveries during the nominal mission of the Mars Science Laboratory in Gale crater, Mars," J. Anal. At. Spectrom. **31**, 863–889 (2016).
4. O. Shoshanim, "Detection of bioaerosols using hyperspectral LIF-LIDAR during S/K challenge II campaign at Dugway," Atmos. Pollut. Res. **14**, 101723 (2023).
5. A. J. Hopkins, J. L. Cooper, L. T. M. Profeta, *et al.*, "Portable deep-ultraviolet (DUV) Raman for standoff detection," Appl. Spectrosc. **70**, 861–873 (2016).
6. Y. Chen, D. C. Morton, and J. T. Randerson, "Remote sensing for wildfire monitoring: insights into burned area, emissions, and fire dynamics," One Earth **7**, 1022–1028 (2024).
7. S. Liu, O. Csillik, E. M. Ordway, *et al.*, "Environmental drivers of spatial variation in tropical forest canopy height: insights from NASA's GEDI spaceborne LiDAR," Proc. Natl. Acad. Sci. U.S.A. **122**, e2401755122 (2025).
8. W. Li, X. Li, Z. Hao, *et al.*, "A review of remote laser-induced breakdown spectroscopy," Appl. Spectrosc. Rev. **55**, 1–25 (2020).
9. J. Lasue, R. C. Wiens, S. M. Clegg, *et al.*, "Remote laser-induced breakdown spectroscopy (LIBS) for lunar exploration," J. Geophys. Res. Planets **117**, 93–102 (2012).
10. S. M. Angel, N. R. Gomer, S. K. Sharma, *et al.*, "Remote Raman spectroscopy for planetary exploration: a review," Appl. Spectrosc. **66**, 137–150 (2012).
11. J. Isaacs, C. Miao, and P. Sprangle, "Remote monostatic detection of radioactive material by laser-induced breakdown," Phys. Plasmas **23**, 033507 (2016).

12. J. D. Strasburg and W. W. Harper, “Impact of atmospheric turbulence on beam propagation,” Proc. SPIE **5413**, 541666 (2004).
13. Y. Guo, Y. Hao, S. Wan, *et al.*, “Direct observation of atmospheric turbulence with a video-rate wide-field wavefront sensor,” Nat. Photonics **18**, 935–943 (2024).
14. L. Allen, M. W. Beijersbergen, R. J. C. Spreeuw, *et al.*, “Orbital angular momentum of light and the transformation of Laguerre-Gaussian laser modes,” Phys. Rev. A **45**, 8185–8189 (1992).
15. A. M. Yao and M. J. Padgett, “Orbital angular momentum: origins, behavior and applications,” Adv. Opt. Photonics **3**, 161–204 (2011).
16. M. J. Padgett, “Orbital angular momentum 25 years on,” Opt. Express **25**, 11265–11274 (2017).
17. W. Cheng, J. W. Haus, and Q. Zhan, “Propagation of vector vortex beams through a turbulent atmosphere,” Opt. Express **17**, 17829–17836 (2009).
18. Z. Chen, C. Li, P. Ding, *et al.*, “Experimental investigation on the scintillation index of vortex beams propagating in simulated atmospheric turbulence,” Appl. Phys. B **107**, 469–472 (2012).
19. J. Ou, Y. Jiang, and Y. He, “Intensity and polarization properties of elliptically polarized vortex beams in turbulent atmosphere,” Opt. Laser Technol. **67**, 1–7 (2015).
20. A. D. Tunick, “The refractive index structure parameter/atmospheric optical turbulence model: CN2,” US Army Research Laboratory Report (1998).
21. L. J. Sjoqvist, O. K. S. Gustafsson, and M. Henriksson, “Laser beam propagation in close vicinity to a down-scaled jet engine exhaust,” Proc. SPIE **5615**, 578291 (2004).
22. S. Oktay, M. Bayraktar, T. E. Tabaru, *et al.*, “Derivation of Rytov variance for jet engine-induced turbulence,” Phys. Scr. **99**, 025516 (2024).
23. M. Krenn, J. Handsteiner, M. Fink, *et al.*, “Twisted light transmission over 143 km,” Proc. Natl. Acad. Sci. U.S.A. **113**, 13648–13653 (2016).
24. W. Yan, Y. Gao, Z. Yuan, *et al.*, “Energy-flow-reversing dynamics in vortex beams: OAM-independent propagation and enhanced resilience,” Optica **11**, 531–541 (2024).
25. W. Yan, Z. Chen, X. Long, *et al.*, “Iso-propagation vortices with OAM-independent size and divergence toward future faster optical communications,” Adv. Photonics **6**, 036002 (2024).
26. J. Wang, J.-Y. Yang, I. M. Fazal, *et al.*, “Terabit free-space data transmission employing orbital angular momentum multiplexing,” Nat. Photonics **6**, 488–496 (2012).
27. Y. Yan, G. Xie, M. P. J. Lavery, *et al.*, “High-capacity millimetre-wave communications with orbital angular momentum multiplexing,” Nat. Commun. **5**, 4876 (2014).
28. Y. Li, K. Morgan, W. Li, *et al.*, “Multi-dimensional QAM equivalent constellation using coherently coupled orbital angular momentum (OAM) modes in optical communication,” Opt. Express **26**, 30969–30977 (2018).
29. M. P. J. Lavery, C. Peuntinger, K. Günthner, *et al.*, “Free-space propagation of high-dimensional structured optical fields in an urban environment,” Sci. Adv. **3**, e1700552 (2017).
30. X. Wang, T. Wu, C. Dong, *et al.*, “Integrating deep learning to achieve phase compensation for free-space orbital-angular-momentum-encoded quantum key distribution under atmospheric turbulence,” Photonics Res. **9**, B9–B17 (2021).
31. L. Wang, W. Jiao, L. Hu, *et al.*, “Residual timing jitter in the free-space optical two-way time and frequency transfer caused by atmospheric turbulence,” Opt. Laser Technol. **163**, 109365 (2023).
32. I. Nape, K. Singh, A. Klug, *et al.*, “Revealing the invariance of vectorial structured light in complex media,” Nat. Photonics **16**, 538–546 (2022).
33. Y. Yuan, J. Zhang, W. Zheng, *et al.*, “Enhanced fiber-coupling efficiency via high-order partially coherent flat-topped beams for free-space optical communications,” Opt. Express **30**, 5634–5643 (2022).
34. W. Wen, X. Mi, and S. Xiang, “Quality factor of partially coherent Airy beams in a turbulent atmosphere,” J. Opt. Soc. Am. A **38**, 1612–1618 (2021).
35. O. J. D. Farley, M. J. Townson, and J. Osborn, “FAST: Fourier domain adaptive optics simulation tool for bidirectional ground-space optical links through atmospheric turbulence,” Opt. Express **30**, 23050–23064 (2022).
36. Z. Zhu, M. Janasik, A. Fyffe, *et al.*, “Compensation-free high-dimensional free-space optical communication using turbulence-resilient vector beams,” Nat. Commun. **12**, 1666 (2021).
37. B. Lu and D. Cai, “Simulation of a temporally dynamic atmospheric wavefront using the modified von-Kármán spectrum and Zernike-based method,” Opt. Express **32**, 38609–38629 (2024).
38. S. Fu and C. Gao, “Influences of atmospheric turbulence effects on the orbital angular momentum spectra of vortex beams,” Photonics Res. **4**, B1–B4 (2016).
39. A. Ghoshroy, J. Davis, A. A. Moazzam, *et al.*, “Enhancing complex light beam propagation in turbulent atmosphere with active convolved illumination,” ACS Photonics **11**, 4541–4558 (2024).
40. O. J. Licht, C. Rohn, and R. Krishna Mohan, “Dynamically adjustable astigmatic transformations for OAM mode identification under atmospheric turbulence,” Opt. Express **33**, 13040–13058 (2025).
41. S. Zaminga, A. Martinez, H. Huang, *et al.*, “Optical chaotic signal recovery in turbulent environments using a programmable optical processor,” Light Sci. Appl. **14**, 131 (2025).
42. E. Karimi, G. Zito, B. Piccirillo, *et al.*, “Hypergeometric-Gaussian modes,” Opt. Lett. **32**, 3053–3055 (2007).
43. H. T. Eyyuboğlu and Y. Cai, “Hypergeometric Gaussian beam and its propagation in turbulence,” Opt. Commun. **285**, 4194–4199 (2012).
44. X. Wang, L. Wang, and S. Zhao, “Research on hypergeometric-Gaussian vortex beam propagating under oceanic turbulence by theoretical derivation and numerical simulation,” J. Mar. Sci. Eng. **9**, 442 (2021).
45. J. Peñano, B. Hafizi, A. Ting, *et al.*, “Theoretical and numerical investigation of filament onset distance in atmospheric turbulence,” J. Opt. Soc. Am. B **31**, 963–971 (2014).
46. L. C. Andrews and R. L. Phillips, “Laser beam propagation through random media,” in *Laser Beam Propagation through Random Media* (SPIE, 2005).
47. F. G. Smith, “Atmospheric propagation of radiation,” in *The Infrared and Electro-Optical Systems Handbook* (SPIE, 1993).
48. B. Yan, D. Li, L. Zhang, *et al.*, “Filamentation of femtosecond vortex laser pulses in turbulent air,” Opt. Laser Technol. **164**, 109515 (2023).
49. C. Peters, V. Cocotos, and A. Forbes, “Structured light in atmospheric turbulence—a guide to its digital implementation: tutorial,” Adv. Opt. Photonics **17**, 113–184 (2025).
50. F. H. Champagne, C. A. Friehe, J. C. Larue, *et al.*, “Flux measurements, flux estimation techniques, and fine-scale turbulence measurements in the unstable surface layer over land,” J. Atmos. Sci. **34**, 515–530 (1977).
51. R. M. Williams and C. A. Paulson, “Microscale temperature and velocity spectra in the atmospheric boundary layer,” J. Fluid Mech. **83**, 547–567 (1977).
52. R. J. Hill, “Models of the scalar spectrum for turbulent advection,” J. Fluid Mech. **88**, 541–562 (1978).
53. L. C. Andrews, “An analytical model for the refractive index power spectrum and its application to optical scintillations in the atmosphere,” J. Mod. Opt. **39**, 1849–1853 (1992).
54. Y. Na and D.-K. Ko, “Adaptive demodulation by deep-learning-based identification of fractional orbital angular momentum modes with structural distortion due to atmospheric turbulence,” Sci. Rep. **11**, 23505 (2021).
55. L. C. Andrews, S. Vester, and C. E. Richardson, “Analytic expressions for the wave structure function based on a bump spectral model for refractive index fluctuations,” J. Mod. Opt. **40**, 931–938 (1993).
56. A. E. Siegman, “How to (maybe) measure laser beam quality,” in *Diode Pumped Solid State Lasers: Applications and Issues* (Optica Publishing Group, 1998).
57. J. H. Churnside, “Aperture averaging of optical scintillations in the turbulent atmosphere,” Appl. Opt. **30**, 1982–1994 (1991).
58. M. A. Khalighi, N. Schwartz, N. Aitamer, *et al.*, “Fading reduction by aperture averaging and spatial diversity in optical wireless systems,” J. Opt. Commun. Netw. **1**, 580–593 (2009).

59. Z. Lin, G. Xu, Q. Zhang, *et al.*, "Scintillation index for spherical wave propagation in anisotropic weak oceanic turbulence with aperture averaging under the effect of inner scale and outer scale," Photonics **9**, 458 (2022).
60. B. Rodenburg, M. Mirhosseini, M. Malik, *et al.*, "Simulating thick atmospheric turbulence in the lab with application to orbital angular momentum communication," New J. Phys. **16**, 033020 (2014).
61. A. Klug, C. Peters, and A. Forbes, "Robust structured light in atmospheric turbulence," Adv. Photonics **5**, 016006 (2023).
62. R. Zhang, N. Hu, K. Zou, *et al.*, "Turbulence-resilient pilot-assisted self-coherent free-space optical communications using automatic optoelectronic mixing of many modes," Nat. Photonics **15**, 743–750 (2021).
63. H. Zhou, X. Su, Y. Duan, *et al.*, "Atmospheric turbulence strength distribution along a propagation path probed by longitudinally structured optical beams," Nat. Commun. **14**, 4701 (2023).
64. B. Zhang, W. Li, J. Chirinos, *et al.*, "Long range propagation of optical vortex beams in atmospheric turbulence," Proc. SPIE **12877**, 128771R (2024).
65. A. E. Willner, P. Kai, H. Song, *et al.*, "Orbital angular momentum of light for communications," Appl. Phys. Rev. **8**, 041312 (2021).
66. M. V. Vasnetsov, I. G. Marienko, and M. S. Soskin, "Self-reconstruction of an optical vortex," J. Exp. Theor. Phys. Lett. **71**, 130–133 (2000).
67. Z. Bouchal, "Resistance of nondiffracting vortex beam against amplitude and phase perturbations," Opt. Commun. **210**, 155–164 (2002).
68. V. Aita, D. J. Roth, A. Zaleska, *et al.*, "Longitudinal field controls vector vortex beams in anisotropic epsilon-near-zero metamaterials," Nat. Commun. **16**, 3807 (2025).
69. D. Session, M. J. Mehrabad, N. Paithankar, *et al.*, "Optical pumping of electronic quantum Hall states with vortex light," Nat. Photonics **19**, 156–161 (2025).
70. Q. Zhou, W. Zhu, L. Chen, *et al.*, "Generation of perfect vortex beams by dielectric geometric metasurface for visible light," Laser Photonics Rev. **15**, 2100390 (2021).
71. B. Liu, Y. He, S. W. Wong, *et al.*, "Multifunctional vortex beam generation by a dynamic reflective metasurface," Adv. Opt. Mater. **9**, 2001689 (2021).
72. C. Zheng, J. Li, J. Liu, *et al.*, "Creating longitudinally varying vector vortex beams with an all-dielectric metasurface," Laser Photonics Rev. **16**, 2200236 (2022).
73. Y. Ming, Y. Intaravanne, H. Ahmed, *et al.*, "Creating composite vortex beams with a single geometric metasurface," Adv. Mater. **34**, 2109714 (2022).
74. M. Liu, P. Lin, P. Huo, *et al.*, "Monolithic silicon carbide metasurfaces for engineering arbitrary 3D perfect vector vortex beams," Nat. Commun. **16**, 3994 (2025).
75. W. Zhao, X. Yi, J. Huang, *et al.*, "All-on-chip reconfigurable generation of scalar and vectorial orbital angular momentum beams," Light Sci. Appl. **14**, 227 (2025).
76. H. Gao, Y. Wang, X. Fan, *et al.*, "Dynamic 3D meta-holography in visible range with large frame number and high frame rate," Sci. Adv. **6**, eaba8595 (2020).
77. M. Agour, E. Kolenovic, C. Falldorf, *et al.*, "Suppression of higher diffraction orders and intensity improvement of optically reconstructed holograms from a spatial light modulator," J. Opt. A Pure Appl. Opt. **11**, 105405 (2009).
78. B. Zhang, K. Meehan, C. Kim, *et al.*, "Simultaneous elimination of zeroth-order and higher-order diffractions in holographic projection with improved energy efficiency and flexibility," Proc. SPIE **28**, PC13879 (2026).
79. S. Lee, J. W. Yoon, J. H. Sung, *et al.*, "Wavefront-corrected high-intensity vortex beams exceeding 1020 W/cm^2," Optica **11**, 1163–1173 (2024).
80. X. Fang, X. Hu, B. Li, *et al.*, "Orbital angular momentum-mediated machine learning for high-accuracy mode-feature encoding," Light Sci. Appl. **13**, 49 (2024).
81. L.-C. Liu, C. Wu, W. Li, *et al.*, "Active optical intensity interferometry," Phys. Rev. Lett. **134**, 180201 (2025).
82. Y. Yuan, T. Lei, S. Gao, *et al.*, "The orbital angular momentum spreading for cylindrical vector beams in turbulent atmosphere," IEEE Photonics J. **9**, 6100610 (2017).
83. J. Wang, "Advances in communications using optical vortices," Photonics Res. **4**, B14–B28 (2016).
84. T. Sarpkaya, R. E. Robins, and D. P. Delisi, "Wake-vortex eddy-dissipation model predictions compared with observations," J. Aircr. **38**, 687–692 (2001).
85. F. H. Proctor, N. N. Ahmad, G. S. Switzer, *et al.*, "Three-phased wake vortex decay," in *AIAA Atmospheric and Space Environments Conference* (2010), pp. 1–12.
86. J. D. Schmidt, *Numerical Simulation of Optical Wave Propagation: with Examples in MATLAB* (SPIE, 2010).
87. J. W. Goodman, *Introduction to Fourier Optics* (Roberts and Company Publishers, 2005).
88. T.-C. Poon and T. Kim, *Engineering Optics with MATLAB* (World Scientific Publishing Co., 2006).
89. W. A. Coles, J. P. Filice, R. G. Frehlich, *et al.*, "Simulation of wave propagation in three-dimensional random media," Appl. Opt. **34**, 2089–2101 (1995).
90. B. M. Welsh, "Fourier-series-based atmospheric phase screen generator for simulating anisoplanatic geometries and temporal evolution," Proc. SPIE **3125**, 279029 (1997).
91. https://github.com/zby0623/Atmospheric-Propagation-Modeling-and-Analysis.